Supplementary Information

Programmable memtransistor array with temporal dynamics modulation for efficient time-series data processing

Dae-won Kim[1], Yoonho Cho[2], Seokho Seo[2], Yujin Kim[2], See-On Park[2], Taehwan Jang[1], Chaebin Park[2], Young Taek Oh[3], Jae-Duk Lee[3] and Shinhyun Choi[1,2]*

[1]Graduate School of Semiconductor Technology, Korea Advanced Institute of Science and Technology (KAIST), Daejeon 34141, Republic of Korea

[2]School of Electrical Engineering, Korea Advanced Institute of Science and Technology (KAIST), Daejeon 34141, Republic of Korea

[3]Semiconductor Research & Development Center, Samsung Electronics, Yongin 17113, Republic of Korea

***Address correspondence to** Shinhyun Choi, Graduate School of Semiconductor Technology, Korea Advanced Institute of Science and Technology (KAIST), Daejeon 34141, Republic of Korea; School of Electrical Engineering, Korea Advanced Institute of Science and Technology (KAIST), Daejeon 34141, Republic of Korea, Email: shinhyun@kaist.ac.kr

Table of Contents

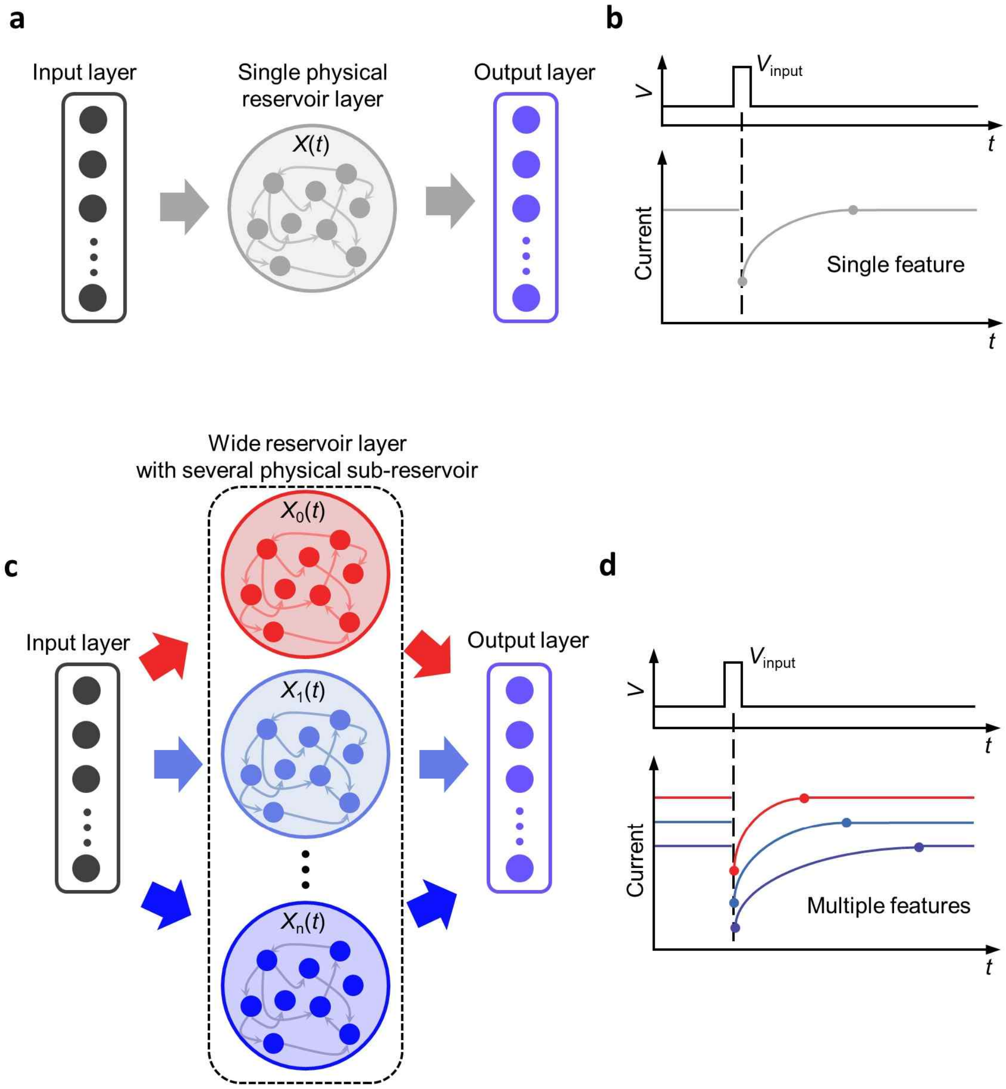

Supplementary Figure 1. Conceptual schematics of the physical reservoir computing systems. **a**, The reservoir computing system with a single physical reservoir layer. **b**, A device for a single reservoir layer generates a single feature from a given input. **c**, The reservoir computing system with a wide physical reservoir layer. **d**, Devices that generate multiple features from the given input can be applied to a physical wide reservoir layer. The multiple carrier dynamics of devices can be utilized as sub-reservoirs[1,2].

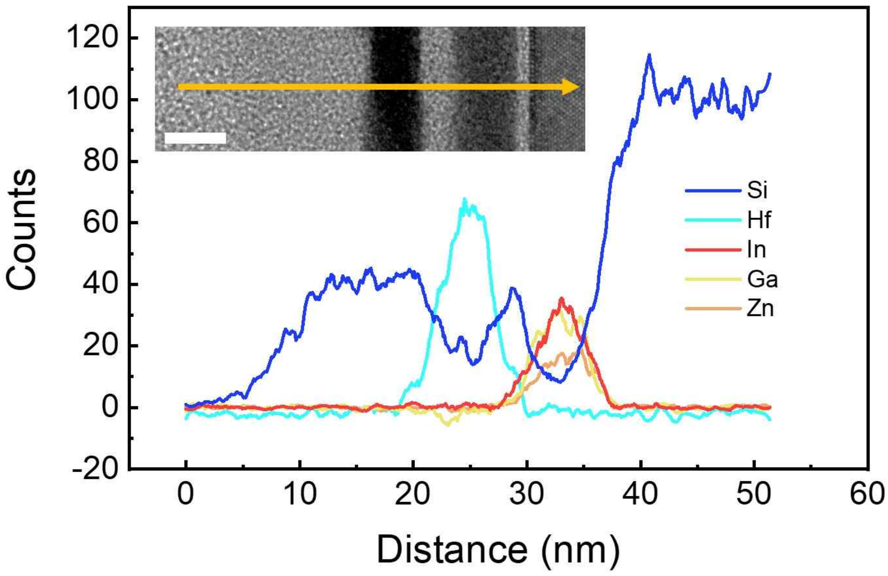

Supplementary Figure 2. Energy dispersive spectroscopy line scanning results of the proposed PDM gate stack. The inset shows the analyzed energy dispersive spectroscopy region and scanning directions. Scale bar, 5 nm.

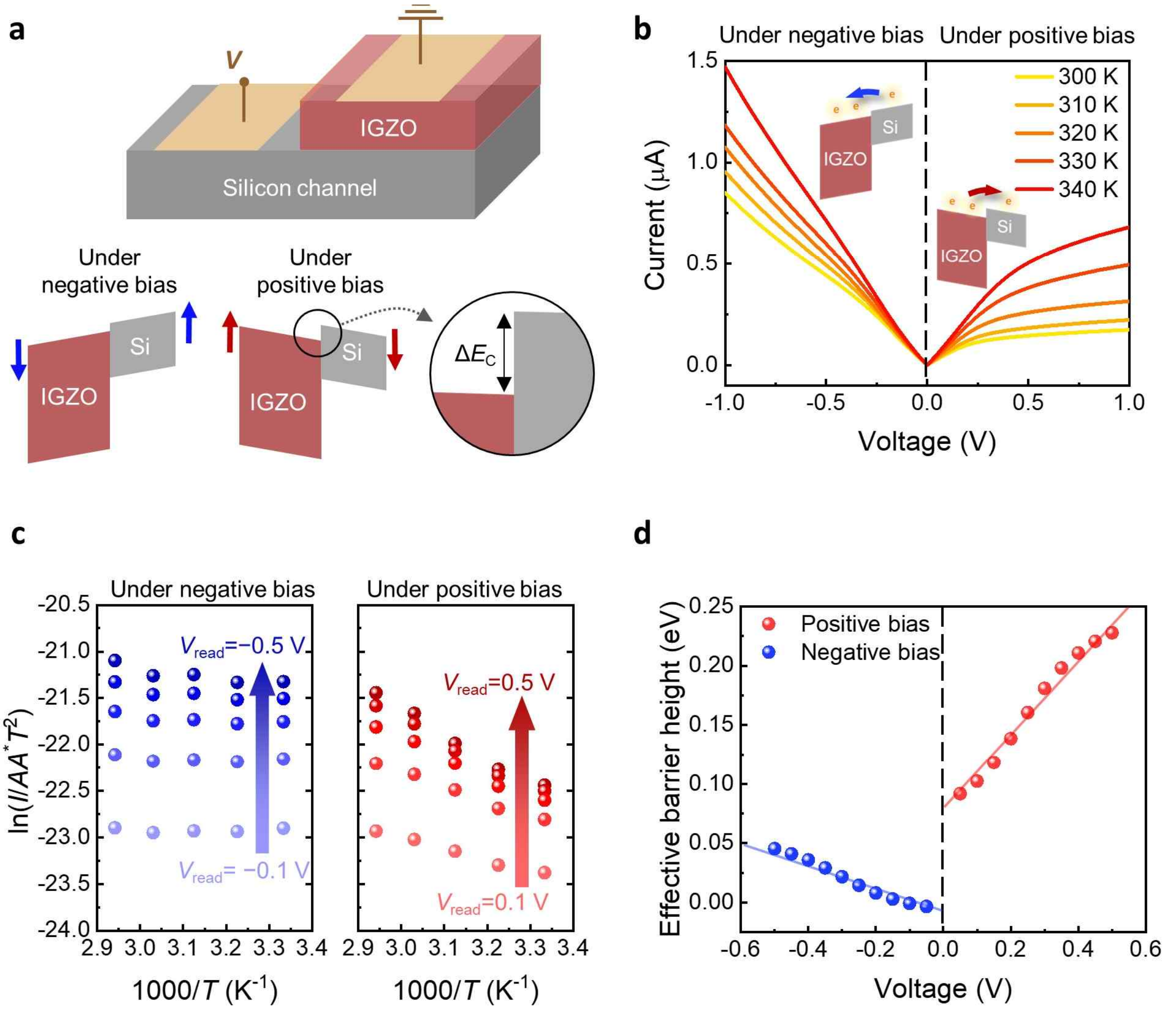

Supplementary Figure 3. Temperature-dependent transport analysis of an IGZO/Si-only test sample with different bias polarity. a, Schematic of the IGZO (5 nm)/Si-only test structure and conceptual band diagrams under positive or negative bias polarities, illustrating a step-wise potential barrier at the interface arising from the IGZO/Si conduction band offset (ΔE_C). **b**, Temperature-dependent current–voltage characteristics (300–340 K) of the test sample, showing polarity-dependent transport asymmetry. **c**, Arrhenius plots, $\ln(I/AA^*T^2)$ versus $1000/T$, extracted at different read voltages under negative bias (left) and positive bias (right), where A is the device area, and A^* is the Richardson constant. **d**, Effective barrier height extracted from the Arrhenius analysis as a function of voltage. The negative-bias side shows a negligible effective barrier, whereas the positive-bias side shows a finite barrier; the near 0 V barrier is approximately 0.08 eV. The voltage-dependent effective barrier height was obtained via linear fitting of temperature-dependent current-voltage data using the thermionic emission model.

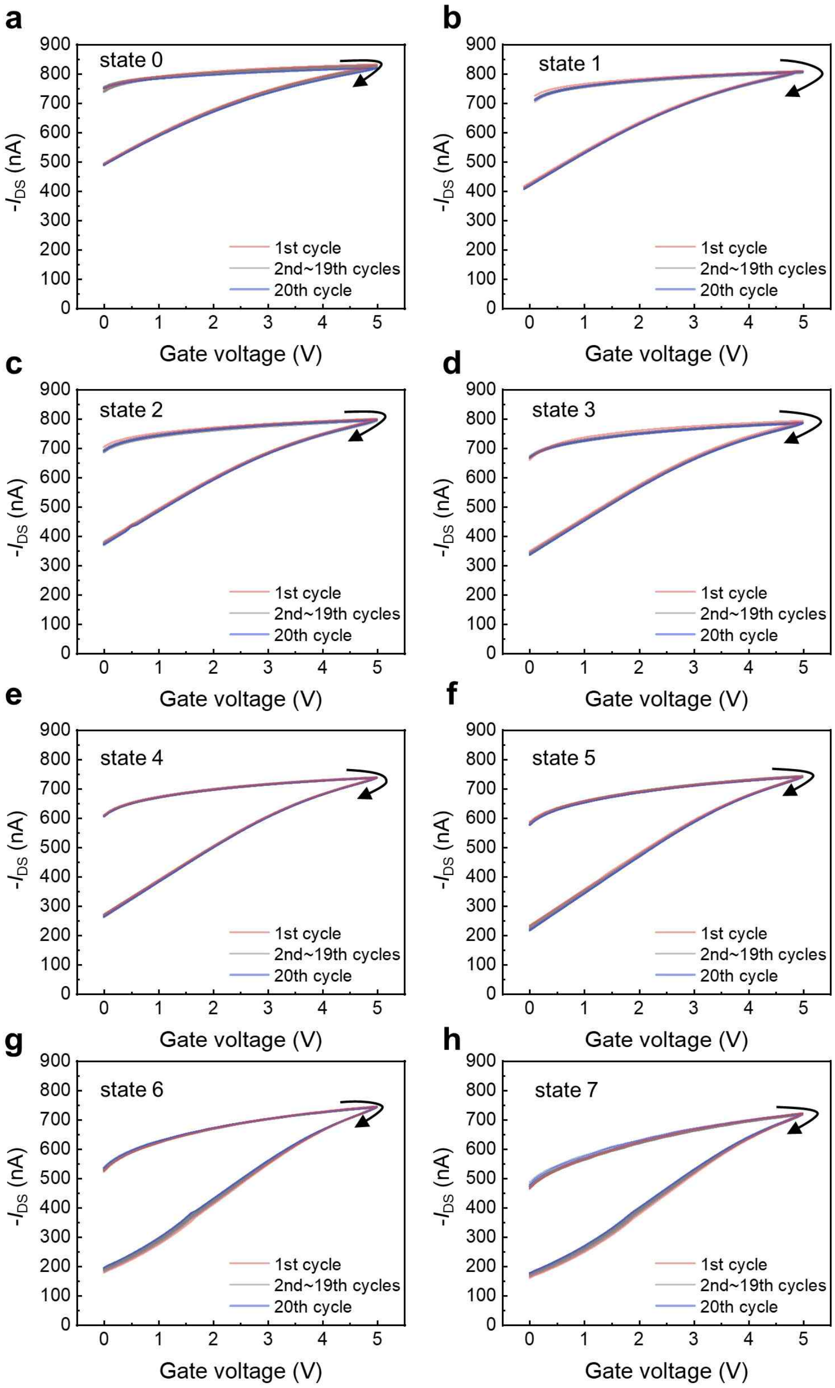

Supplementary Figure 4. Volatile switching characteristics under repeated double-sweep measurements for different CTL-programmed states. Measured drain current–gate voltage curves for **a**, state 0 (V_{Prog} = -16 V) **b**, state 1 (V_{Prog} = 14 V) **c**, state 2 (V_{Prog} = 15 V) **d**, state 3 (V_{Prog} = 16 V) **e**, state 4 (V_{Prog} = 17 V) **f**, state 5 (V_{Prog} = 18 V) **g**, state 6 (V_{Prog} = 19 V) **h**, state 7 (V_{Prog} = 20 V). Measured curves were measured at V_{DS} = −2.5 V with the source grounded. The gate voltage was applied as a double sweep voltage from 0 to 5 V and back to 0 V with a cycle-to-cycle interval of 1 s. In each panel, the 1st cycle is shown in a red line, the 2nd–19th cycles are shown in gray lines, and the 20th cycle is shown in a blue line. All states exhibit hysteresis with volatile recovery toward the initial drain current level after returning to gate voltage = 0 V.

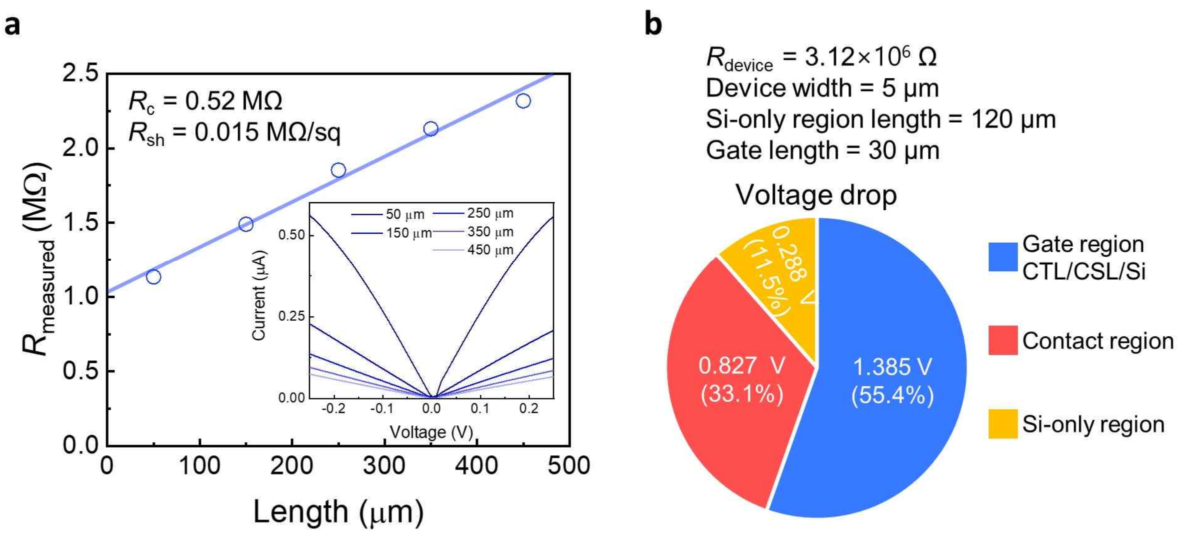

Supplementary Figure 5. Transmission line method-based analysis of resistance/ potential drop in the PDM device. a, Transmission line method (TLM) analysis plot of total resistance versus channel length. The inset shows current–voltage curves measured with different pad spacings. **b**, Device resistance/potential-drop partition estimated from the TLM parameters and device geometry, showing contributions from the gated region (CTL/CSL/Si), contact region ($2R_c$), and Si-only region.

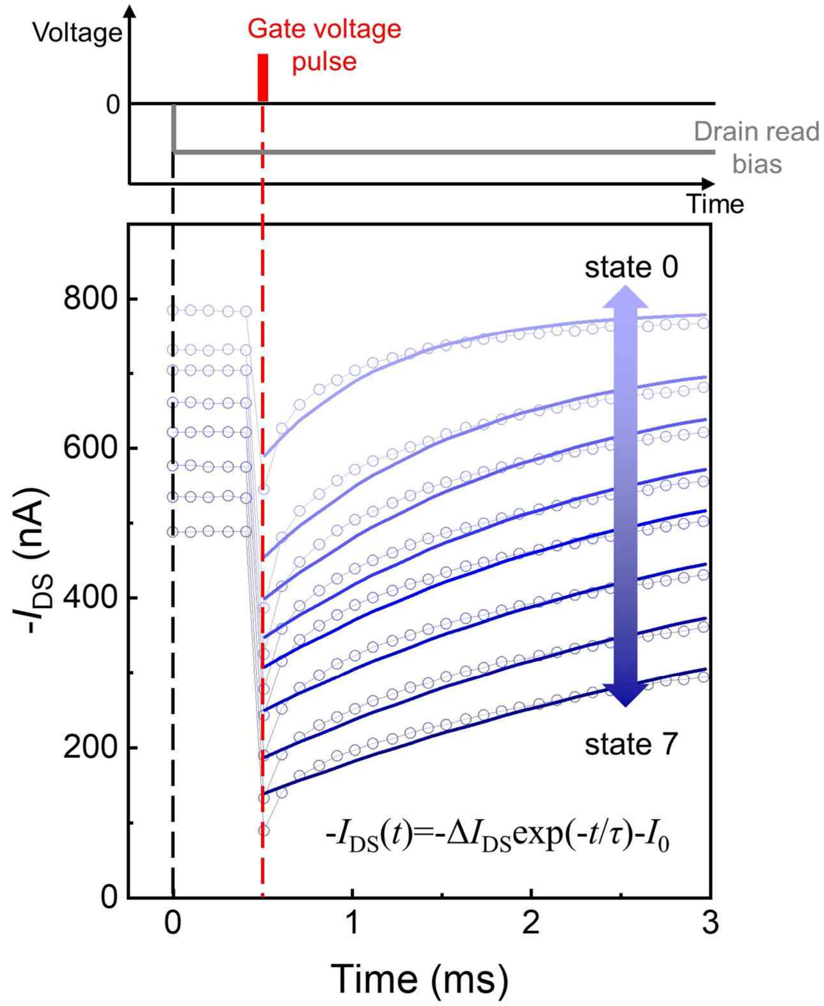

Supplementary Figure 6. Single exponential fitting procedure for extracting the relaxation time constant. As a representative example, a gate-voltage pulse (5 V, 150 ns) is applied while a constant drain read bias (-2.5 V) is maintained, and the drain current is sampled with a 100 μs interval. Open symbols denote experimentally measured drain current, and solid lines denote the corresponding single exponential fit, from which the $-I_0$ is the base current and τ is the relaxation time constant. Curves for all 8 CTL-programmed states are shown. The fitting quality is quantified by the coefficient of determination (R^2), with an average R^2 of 0.93 across the CTL-programmed states.

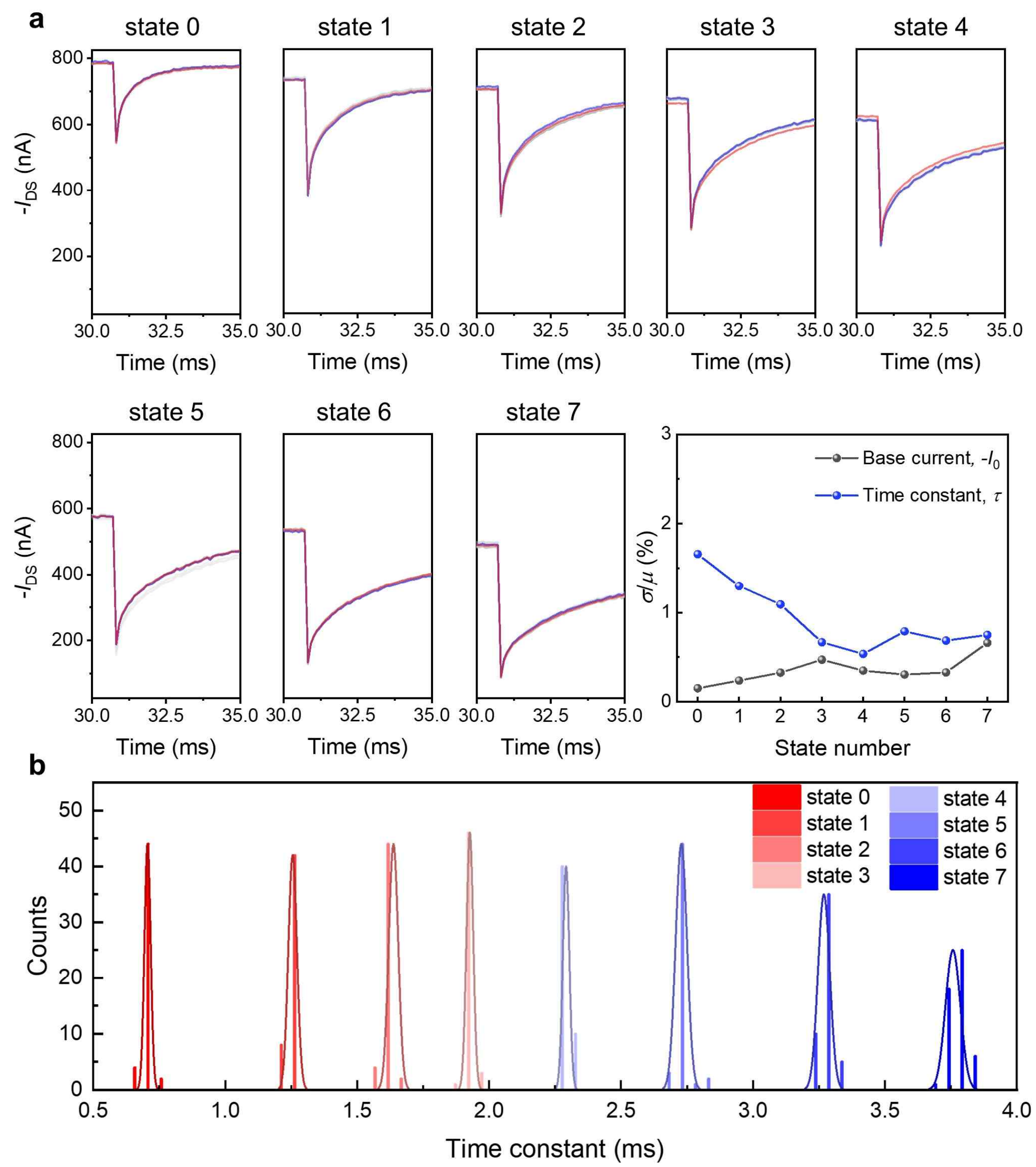

Supplementary Figure 7. Cycle variation and probability distribution of single pulse relaxation dynamics across CTL-programmed states. a, The drain current transient responses to a single gate pulse (5 V, 150 ns) measured for 50 repeated cycles at each CTL-programmed state (V_{DS} = −2.5 V, source grounded; sampling interval: 100 µs). The 1st cycle is shown in red, cycles 2nd–49th in gray, and the 50th cycle in blue. Cycle variations of the extracted base current and relaxation time constant are also summarized, where σ and μ denote the standard deviation and mean, respectively. **b**, Probability distributions of the extracted relaxation time constants over 50 cycles for each CTL-programmed state, showing preserved state-dependent separation with finite cycle variation.

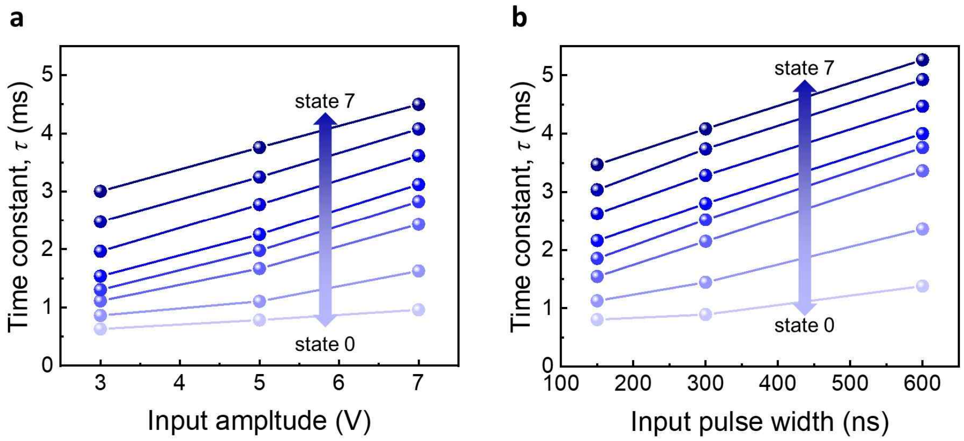

Supplementary Figure 8. The input pulse effect for temporal dynamics modulation. Pulse-condition dependence of the state-dependent temporal, measured for 8 CTL-programmed states under the indicated gate pulse conditions, for gate pulse amplitude (fixed pulse width of 150 ns) **a**, and gate pulse width (fixed pulse amplitude of 5 V) **b**, confirming that the state-dependent temporal dynamics are preserved across different input pulses. The drain current transient responses were measured with $V_{DS} = -2.5$ V (source grounded; sampling interval: 100 µs).

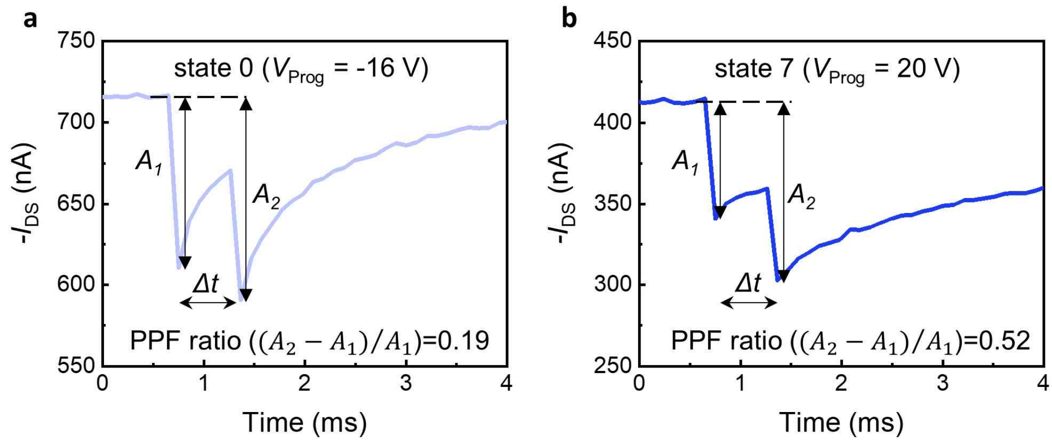

Supplementary Figure 9. PPF effects at different CTL-programmed states. A pair of pulses stimulation response of **a**, CTL erased states (state 0) and **b**, CTL-programmed states (state 7). In both cases, a pair of pulses was applied (3 V, 150 ns with an interval of 600 µs) to evaluate the temporal cumulative effects[3]. The drain current transient responses were measured with $V_{DS} = -2.5$ V (source grounded; sampling interval: 100 µs).

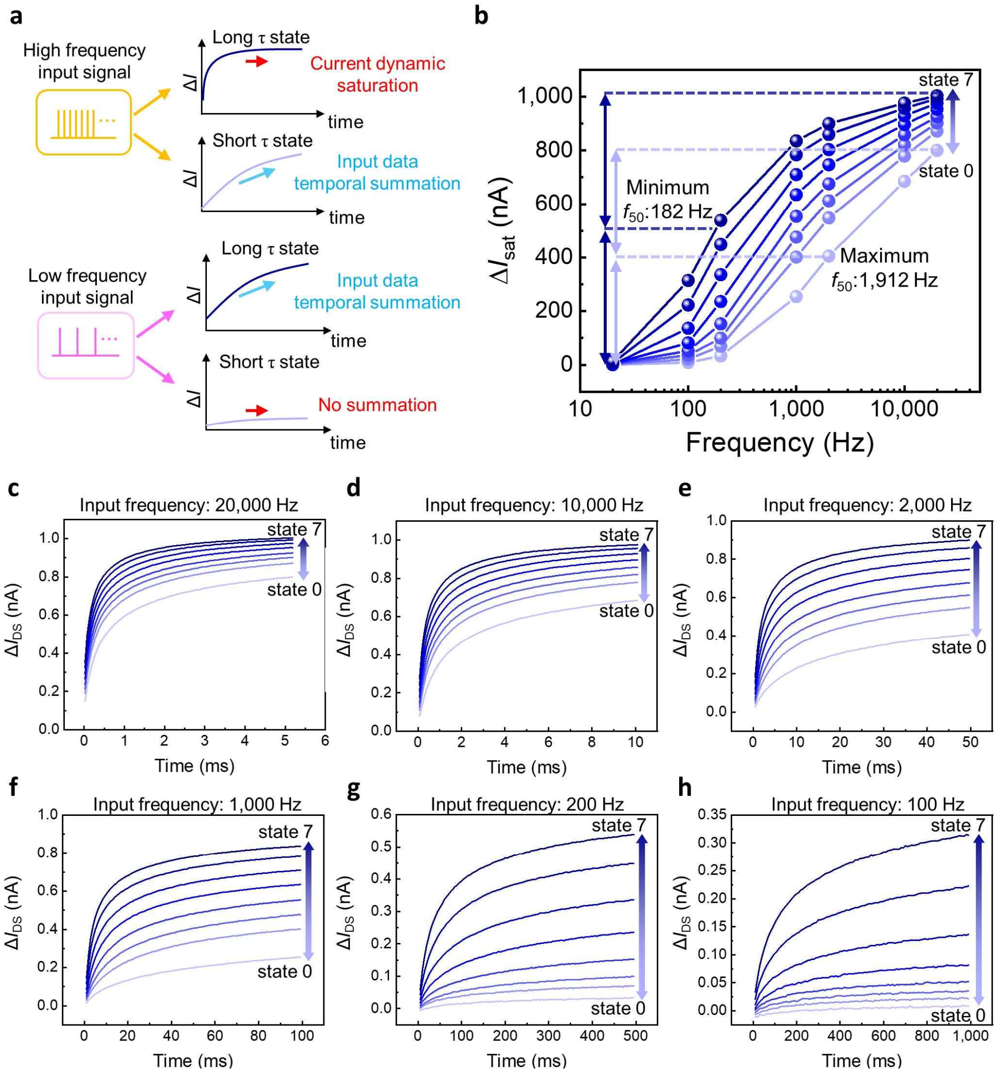

Supplementary Figure 10. Frequency-response analysis of the PDM under pulse train stimulation with varying CTL-programmed states. a, Conceptual illustration of frequency-dependent temporal summation and relaxation in short- and long-τ states under different input frequencies. At intervals much shorter than the relaxation timescale, little relaxation occurs between pulses, so summation dominates until the current change approaches saturation. At longer intervals, relaxation suppresses summation. When the interval is comparable to the relaxation timescale, the current change accumulates progressively through a balance between summation and relaxation. **b**, Frequency dependence of the saturation-depth metric, ΔI_{sat}, for CTL-programmed states 0–7. 100 gate pulses (3 V, 150 ns) were applied while varying only the pulse interval, with input frequency defined as the inverse of the interval. Measurements were performed at discrete frequencies from 20 to 20,000 Hz. ΔI_{sat} was defined as the difference between the initial and post-sequence drain current magnitudes, providing a measure of the balance between temporal summation and relaxation. From the ΔI_{sat}–frequency curves, the characteristic transition frequency, f_{50}, was extracted as the frequency at which ΔI_{sat} reaches 50% of its total change between the low-frequency (20 Hz) and high-frequency (20,000 Hz) limits. The extracted f_{50} values range from 182 to 1,912 Hz across the programmed states, indicating that CTL programming shifts the characteristic temporal-response window over approximately one decade in frequency. This f_{50} range represents a condition-dependent response window extracted under the present pulse-train condition, rather than a universal bandwidth limit of the PDM. Accordingly, these characteristic frequencies should be interpreted within the present measurement protocol and may vary with input pulse condition, read bias, sampling condition, and response metric. **c**–**h**, Transient drain current changes (ΔI_{DS}) of states 0–7 under the same 100 pulses stimulation at representative input frequencies of **c**, 20,000, **d**, 10,000, **e**, 2,000, **f**, 1,000, **g**, 200, and **h**, 100 Hz, respectively. The drain-current transients were measured at V_{DS} = −3 V with the source grounded, and sampled 50 μs after each gate pulse. At 20 Hz (5 ms interval), no appreciable current change was observed for any programmed state.

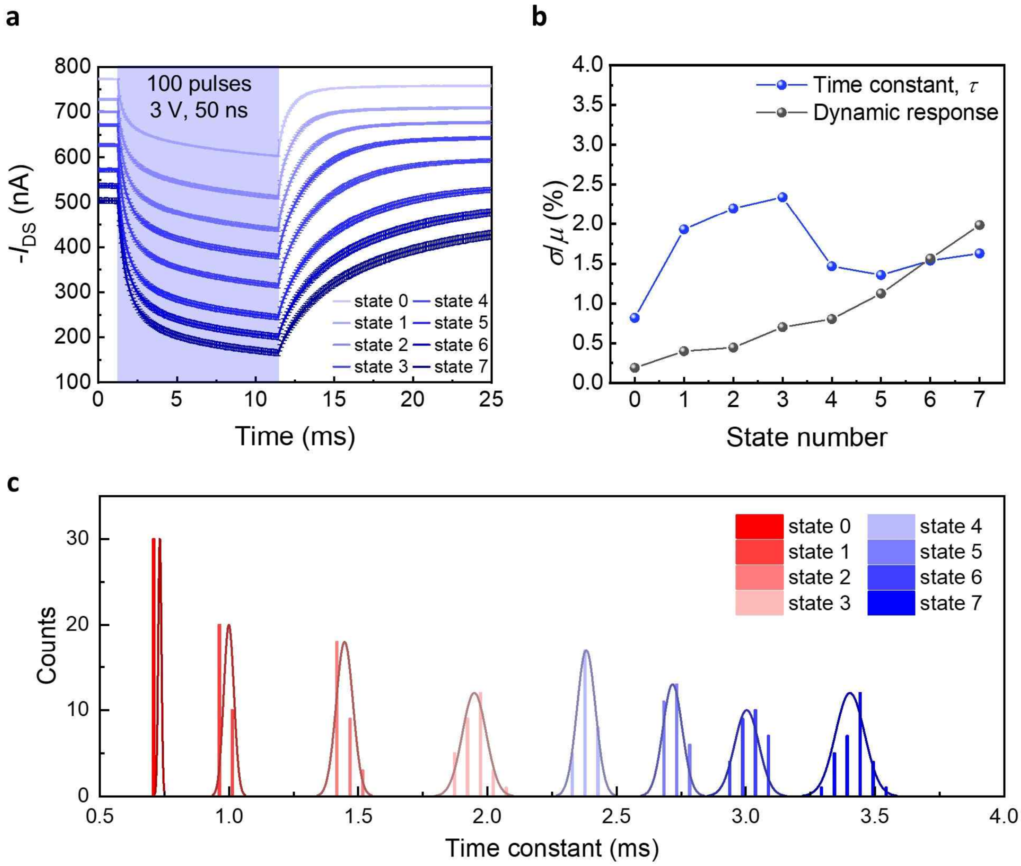

Supplementary Figure 11. Cycle variation analysis of the programmed temporal dynamics under repeated high-speed volatile switching. **a**, Repeated transient drain current responses measured for 30 cycles for each CTL-programmed state (states 0–7). For the measurements, the gate pulse train (3 V, 50 ns, 100 pulses at 10 kHz) was applied, and the temporal dynamics were monitored without gate pulse stimulation, under a constant drain read bias (V_{DS} = −2.5 V) with a current sampling interval of 100 μs. The solid lines are presented as mean current values with error bars indicating standard deviation. **b**, Cycle variation of the relaxation time constant (τ) and dynamic current response as a function of CTL-programmed state. The τ is extracted after the 100 gate pulse train. **c**, Extracted τ for 30 cycles at each programmed state, showing preserved state-dependent separation with finite cycle variation.

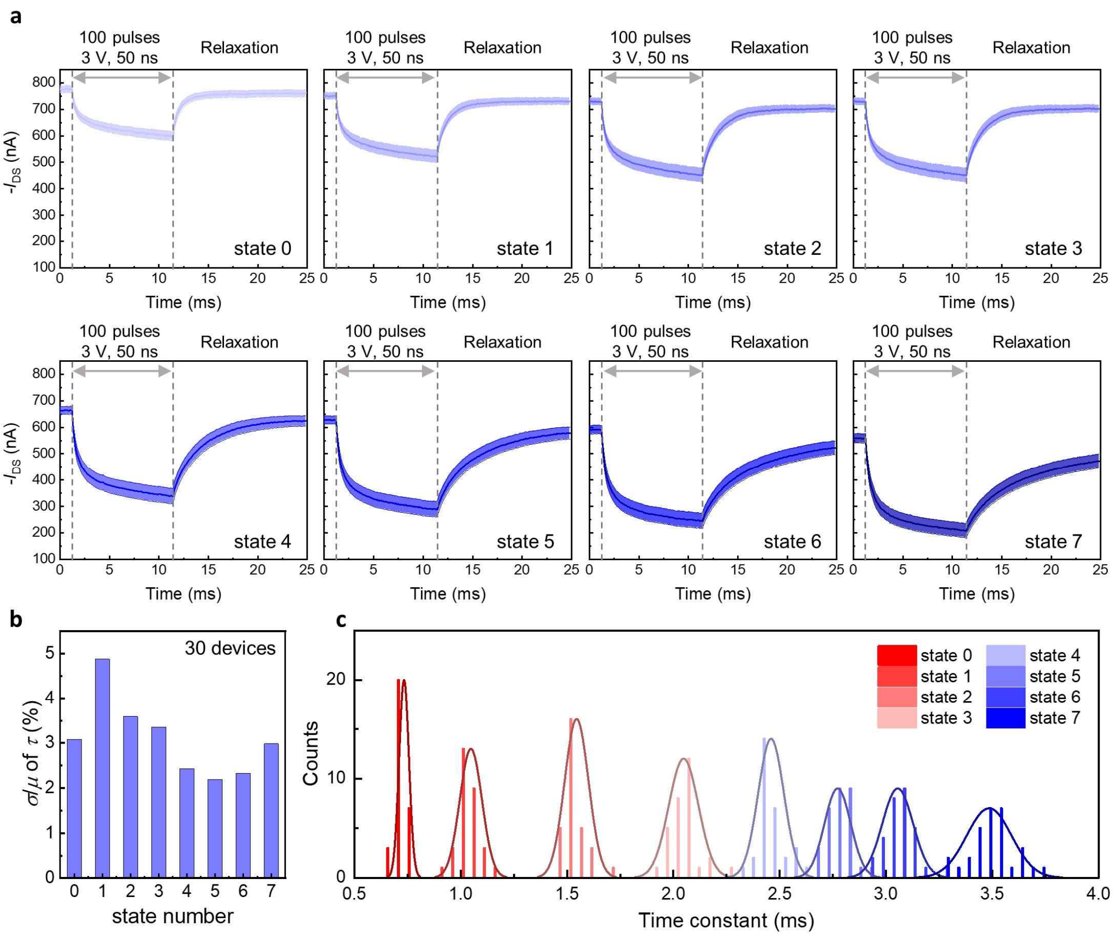

Supplementary Figure 12. Device variation analysis supporting the 8 CTL-programmed states operation. a, Representative drain current relaxation responses for all 8 CTL-programmed states (states 0–7), showing state-dependent temporal dynamics. The mean current is shown as a solid line, and the shaded region indicates the standard deviation across devices. **b**, Extracted device variation of time constants (τ) measured across 30 devices for each CTL-programmed state, showing state-wise variation within <5% (σ/μ). **c**, Probability distributions of τ for each CTL-programmed state, indicating finite spread with limited overlap between adjacent states while preserving overall state-dependent ordering. For the measurements, the gate pulse train (3 V, 50 ns, 100 pulses at 10 kHz) was applied, and the temporal dynamics were monitored without gate pulse stimulation, under a constant drain read bias (V_{DS} = −2.5 V) with a current sampling interval of 100 µs. Before measurements, all devices were applied by a CTL erase pulse (-16 V, 50 ms).

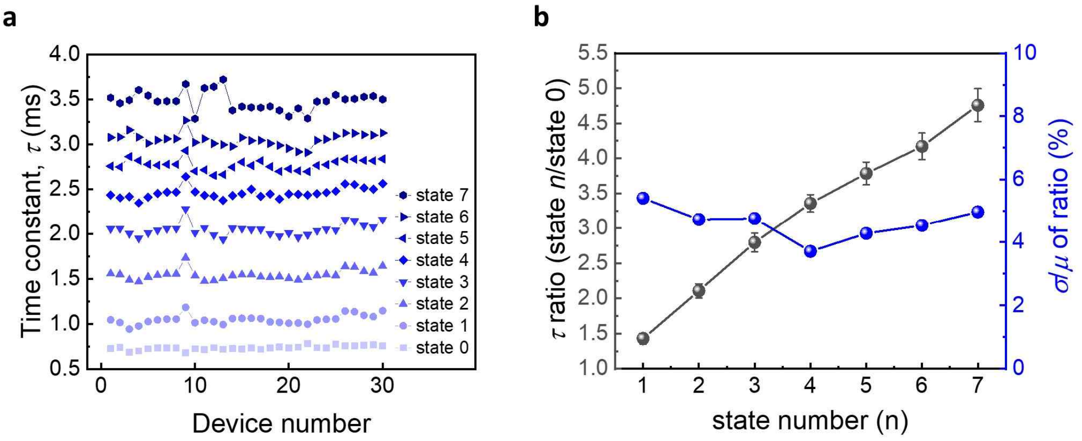

Supplementary Figure 13. Statistical analysis of CTL-programmed temporal dynamics modulation and device across 30 devices. a, Absolute τ values extracted for each CTL-programmed state (states 0–7) across the measured device set, highlighting that the programmable τ span (state 0 to state 7). **b**, Device-normalized τ modulation ratios (τ at state n divided by τ at state 0) across the same device set, showing consistent state-dependent τ modulation with <5% variation across devices.

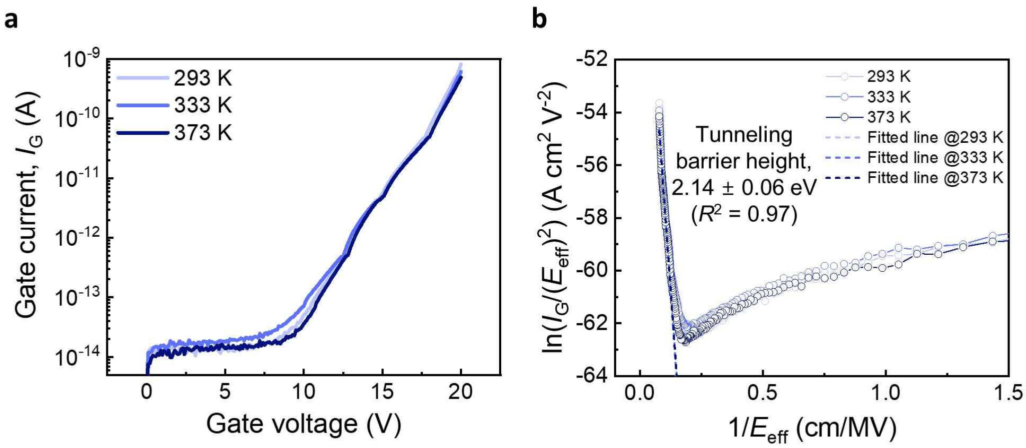

Supplementary Figure 14. Temperature-dependent gate current analysis of CTL programming. a, Gate leakage current as a function of gate voltage measured at 293, 333, and 373 K, showing weak temperature dependence under the programming-bias range. **b**, Fowler–Nordheim (F–N) plots of $\ln(I_G/(E_{eff})^2$ versus $1/E_{eff}$ at 293, 333, and 373 K with linear fitting. The effective tunneling field, E_{eff}, was defined as the electric field across the 3 nm SiO_2 tunneling oxide using a dielectric-divider approximation for the gate stack. The extracted effective barrier height is 2.14±0.06 eV, indicating F–N tunneling behavior with trap-assisted tunneling contributions.

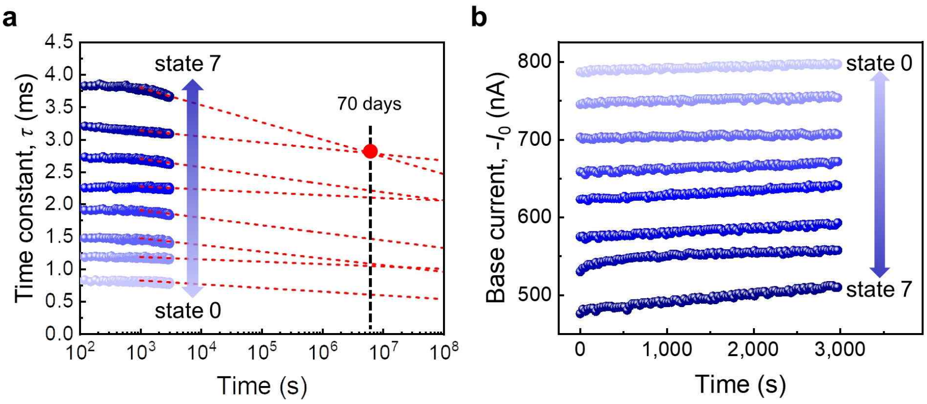

Supplementary Figure 15. Retention analysis of programmed temporal dynamics states. **a**, Time constant (τ) versus time for CTL-programmed states (states 0–7). Blue symbols indicate the measured τ values, and red dashed lines indicate semi-log fitting/extrapolation lines (τ versus log(time)); the fitting was performed from 1000 s. The extrapolated trend indicates a gradual reduction of state separability over extended times, with adjacent high states (e.g., states 6 and 7) expected to overlap first at approximately the 70-days timescale. **b**, A retention characteristic of base current with multiple CTL-programmed states. To evaluate the retention characteristics of temporal dynamics modulation, the CTL was programmed and subsequently stimulated with a single pulse (5 V, 150 ns) applied at 30-second intervals over a total duration of 3,000 seconds. The drain bias of – 2.5 V was applied to read the transient responses of PDM.

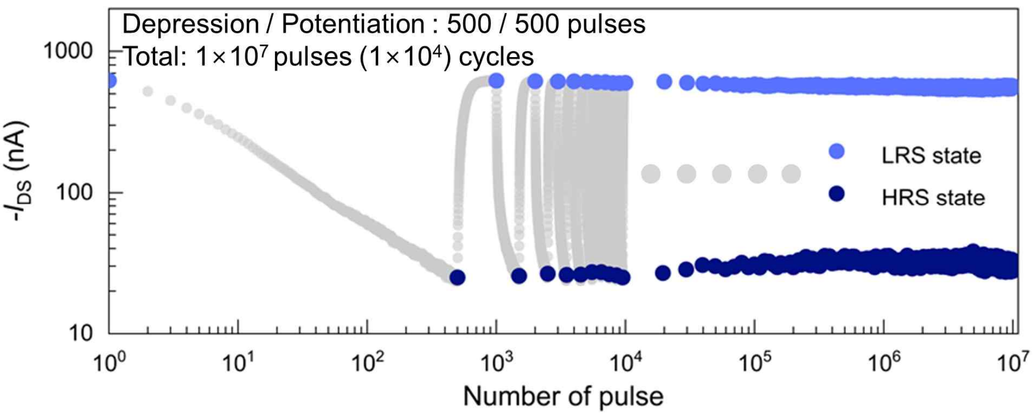

Supplementary Figure 16. Endurance of volatile switching at the most-programmed condition (state 7). Endurance of volatile resistive switching at the state 7, measured using the same endurance test condition as Figure 2h (500 depression pulses at 5 V, 500 ns followed by 500 potentiation pulses at −5 V, 50 µs per cycle; read by a −2.5 V, 20 µs drain pulse applied 1 µs after each switching pulse), confirming stable operation over 1×10^7 pulses, with cycle variation coefficients of σ/μ = 1.8% (LRS) and 5.6% (HRS).

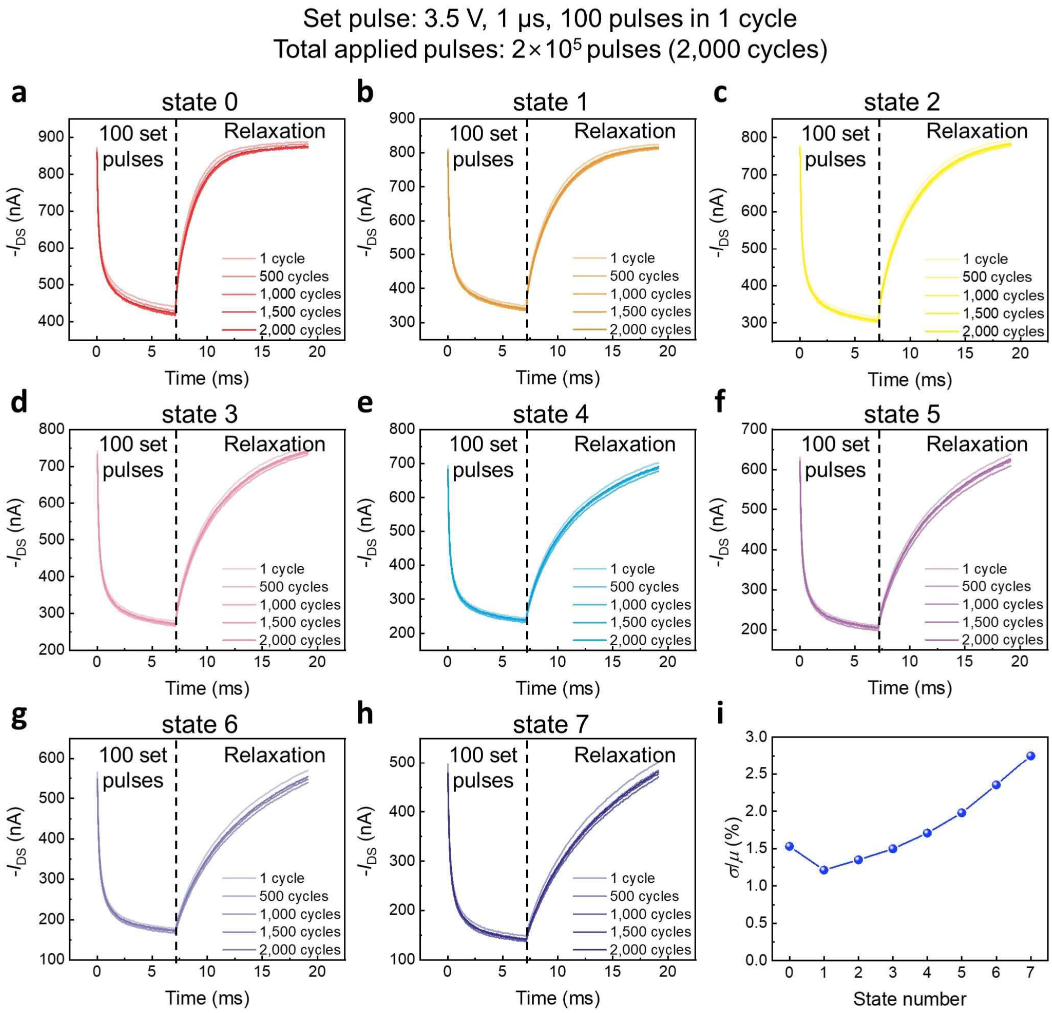

Supplementary Figure 17. Cycle stability of volatile temporal dynamics across all CTL-programmed states. a–h, The drain current transients were measured for 8 CTL-programmed states (states 0–7) under a repeated gate-sequence characterization protocol. In each characterization cycle, the device was driven by 100 gate set pulses (3.5 V, 1 μs, interval 71 μs) followed by a 0 V gate voltage relaxation window (100 segments, 50 μs each), while drain read pulses (−2.5 V, 50 μs) were applied with a fixed delay (10 μs) after each gate segment to monitor the volatile response. Panels show the measured responses at selected cycle counts (1, 500, 1000, 1500, and 2000 cycles). **i**, The corresponding cycle variation of the current dynamic, indicating only limited degradation (<3%) over the tested cycling window.

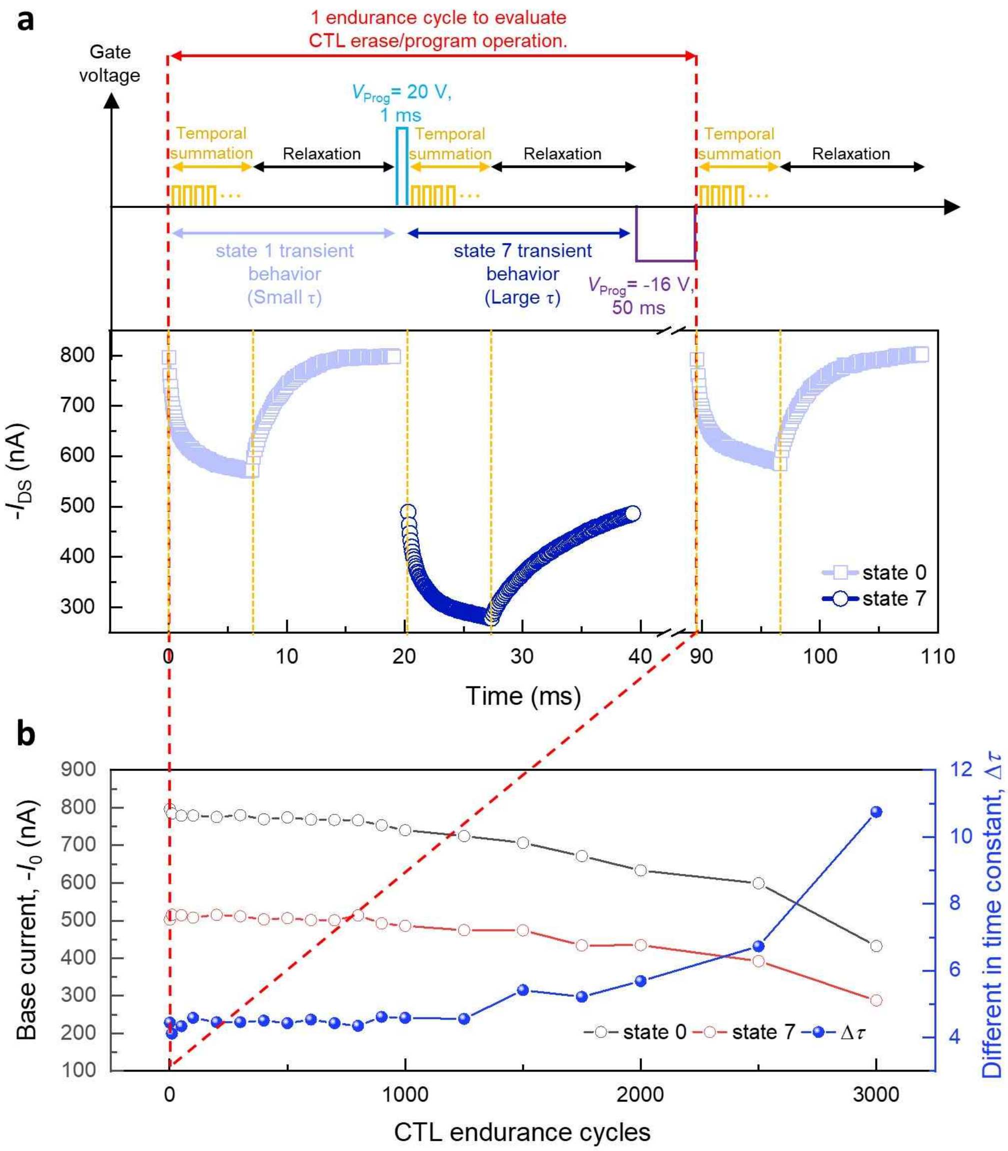

Supplementary Figure 18. Endurance of volatile temporal dynamics under repeated CTL erase/program cycling. a, Measurement protocol for stress-cycling between the CTL-erased state (state 0; −16 V, 50 ms) and the most-programmed state (state 7; 20 V, 1 ms), with periodic volatile-dynamics characterization inserted between CTL operations. The volatile characterization uses a gate sequence of 100 set pulses (3 V, 1 µs, interval 70 µs) followed by a 0 V relaxation window (total 100 segments, each 50 µs), while the drain current is monitored by a read pulse (−2.5 V, 50 µs) applied at a fixed delay (10 µs) after each gate segment. **b**, Extracted base current (first readout value after each CTL erase/program operation) and time-constant difference ($\Delta\tau$ between erased and programmed conditions) as a function of endurance cycling count, showing stable behavior up to 1,000 cycles.

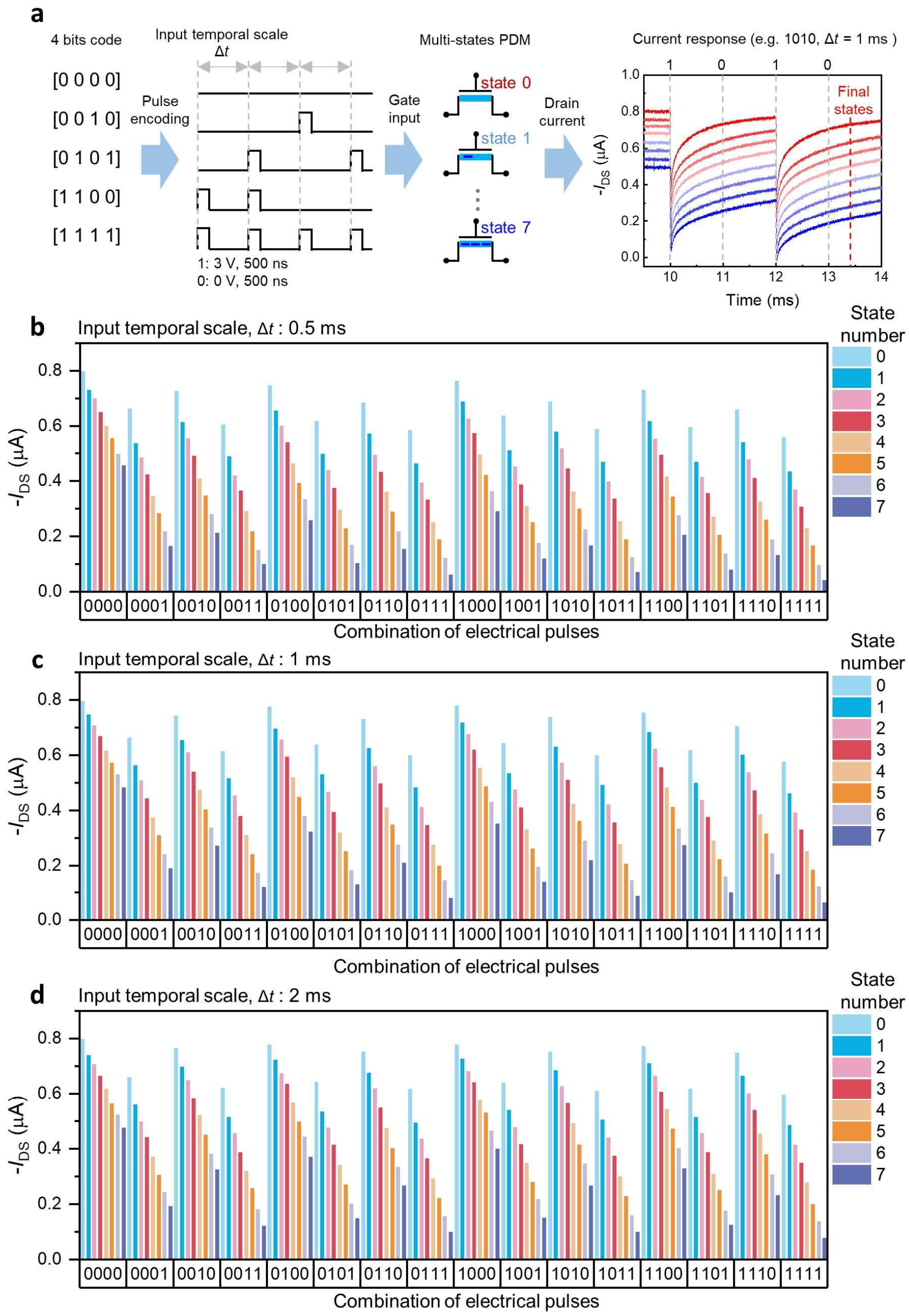

Supplementary Figure 19. 4-bit temporal-input characterization for input temporal scale, Δ*t* = 0.5–2 ms. a, Measurement concept for 4-bit characterization. A 4-bit input sequence (0000–1111) is applied to the PDM, where each bit is encoded as a 3 V, 500 ns gate pulse ("1") or a 0 V, 500 ns gate pulse ("0"), with input temporal scale, Δ*t*, between successive pulses. The PDM current is measured at a drain bias of −2.5 V, and the readout value is taken at a fixed delay of 450 μs after the 4th pulse. Measured current-response distributions for the 16 input sequences across the 8 CTL-programmed states for Δ*t* = 0.5 ms **b**, 1 ms **c**, and 2 ms **d**, respectively.

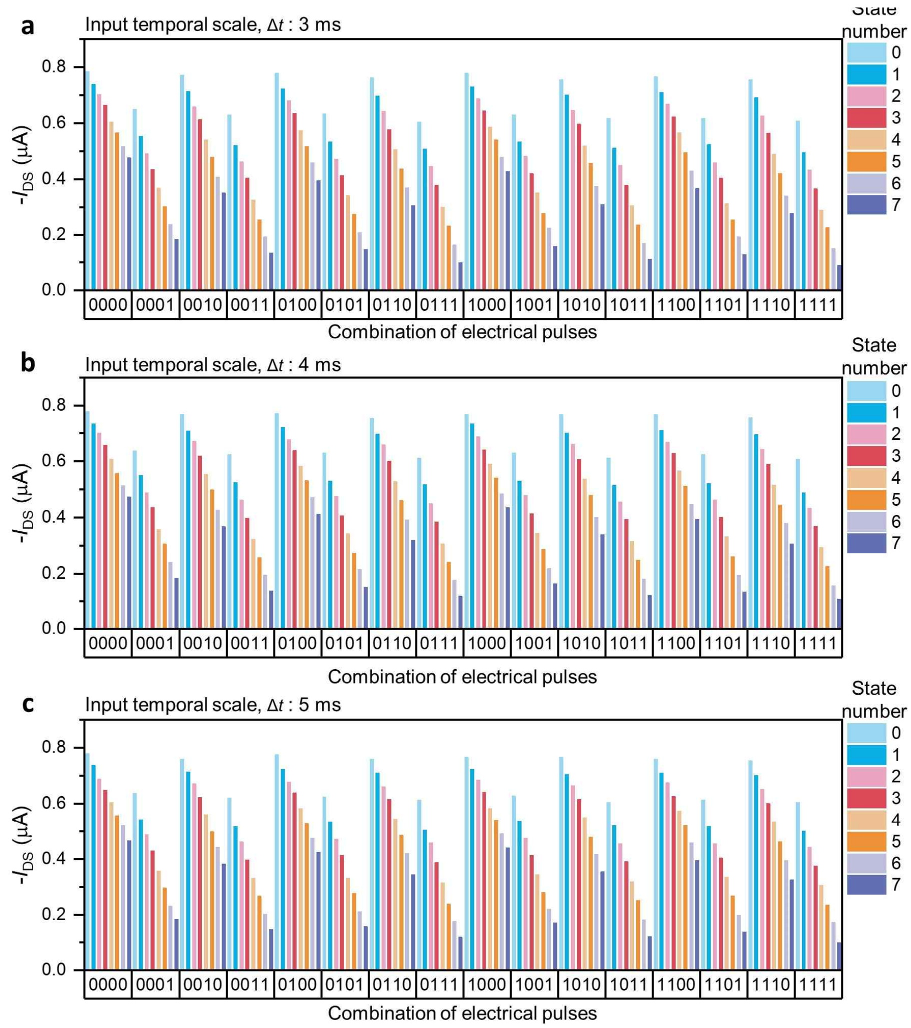

Supplementary Figure 20. 4-bit temporal-input characterization at longer input temporal scale (Δt = 3–5 ms). Measured current-response distributions for the 16 input sequences across the 8 CTL-programmed states at the fixed 450 μs read delay for Δt = 3 ms **a**, 4 ms **b**, and 5 ms **c**, respectively.

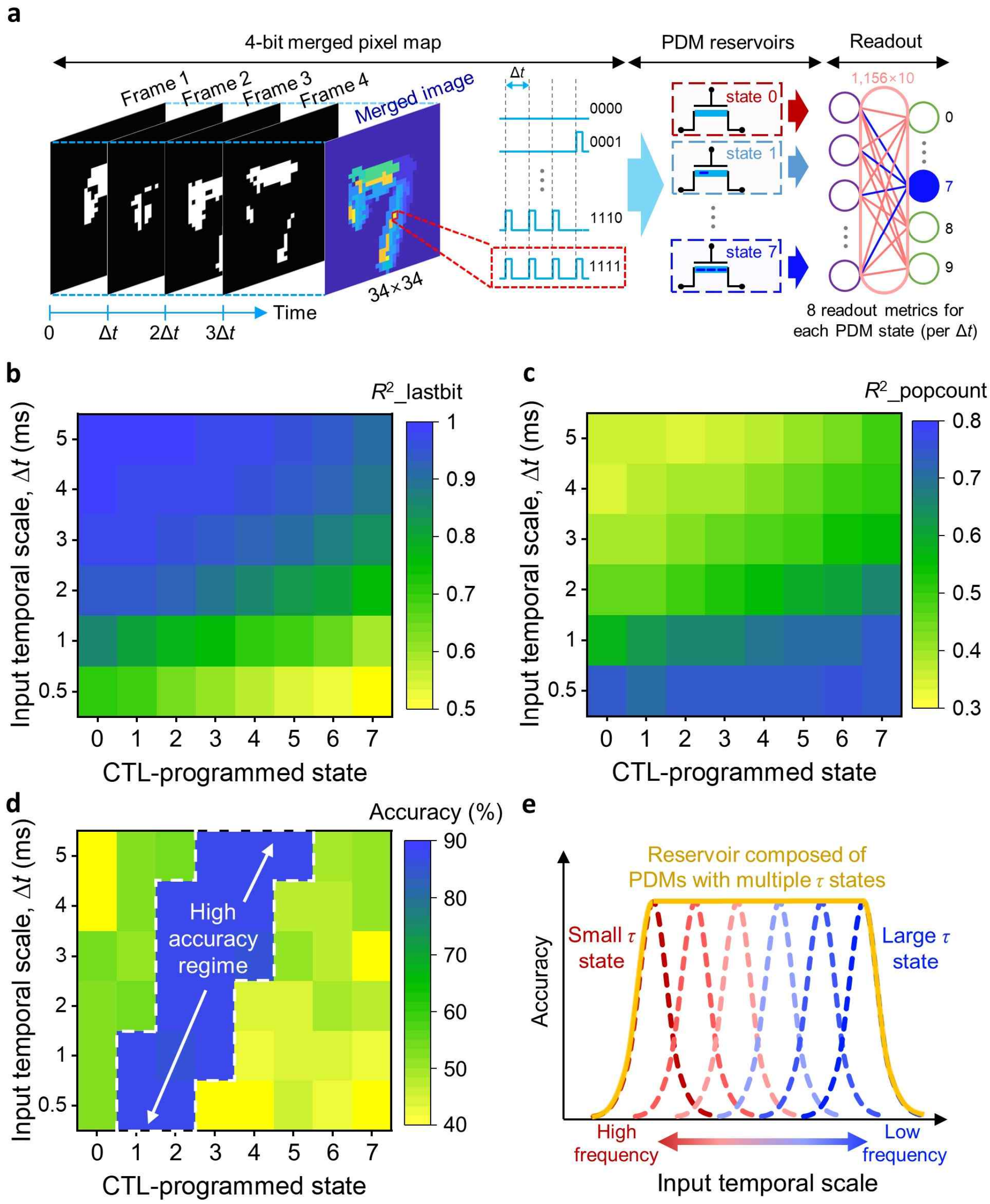

Supplementary Figure 21. N-MNIST evaluation pipeline and Δ*t*/state-dependent information-processing and accuracy trends. **a**, Schematic of the N-MNIST evaluation pipeline. **b**, Heat map of R^2 for the last-bit-only model (R^2_lastbit) calculated from the experimentally measured 16-sequence responses, quantifying the degree of last-bit (4th frame) dominance. **c**, Heat map of R^2 for the popcount-only model (R^2_popcount) calculated from the same experimentally measured 16-sequence responses, quantifying the degree of popcount-dominated (order-insensitive) behavior. **d**, N-MNIST classification-accuracy heat map across Δ*t* and CTL-programmed states. **e**, Conceptual schematic showing that a reservoir composed of PDMs spanning a wide range of programmed time constants can cover diverse input temporal scales and thereby enable multiscale temporal feature extraction with robust classification performance across temporally diverse datasets.

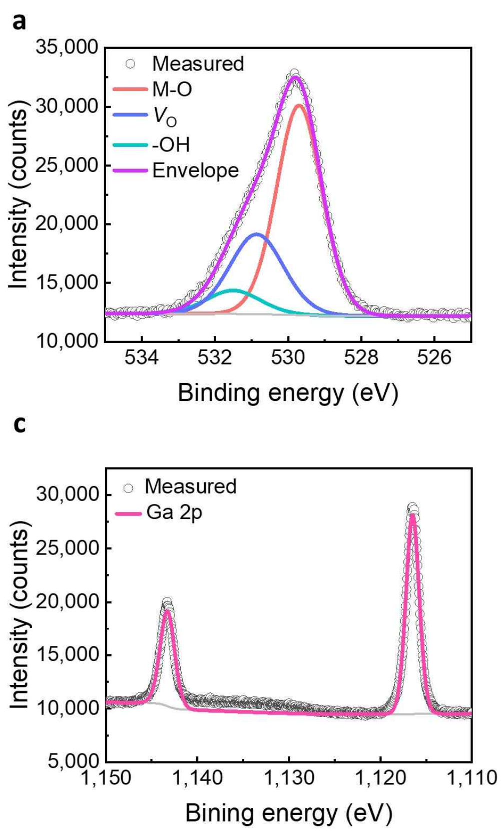

Supplementary Figure 22. The XPS profile of IGZO for CSL. XPS spectra results of IGZO for **a**, O 1*s*. **b**, In 3*d*. **c**, Ga 2*p*. **d**, Zn 2*p*. Oxygen vacancies (V_O) related XPS peak was detected in O 1s XPS spectra of IGZO film[4].

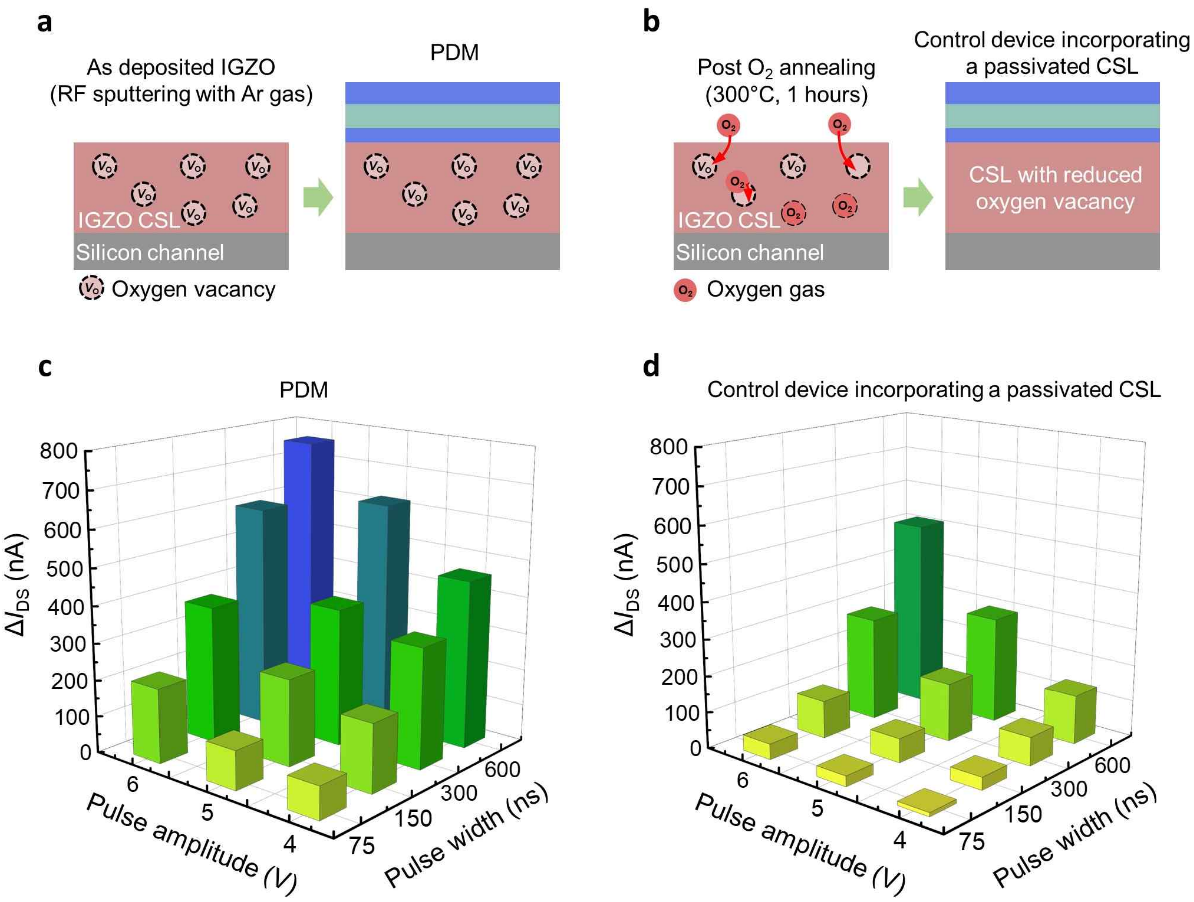

Supplementary Figure 23. Post O_2 annealing effects on CSL to examine the role of oxygen vacancy-related defects in the temporal dynamics. **a**, Schematic illustration of the PDM device incorporating the as-deposited IGZO CSL and **b**, the control device incorporating a post-O_2 annealed (passivated) CSL with reduced oxygen vacancies. **c**, ΔI_{DS} of the PDM device measured as a function of pulse amplitude and pulse width. **d**, ΔI_{DS} of the control device with the passivated CSL, showing significantly suppressed current dynamics[12]. This result supports the contribution of oxygen vacancy-related bulk defects to the temporal dynamics, while the overall trap-mediated response may also include possible interface trap contributions that are not quantitatively separated in this analysis.

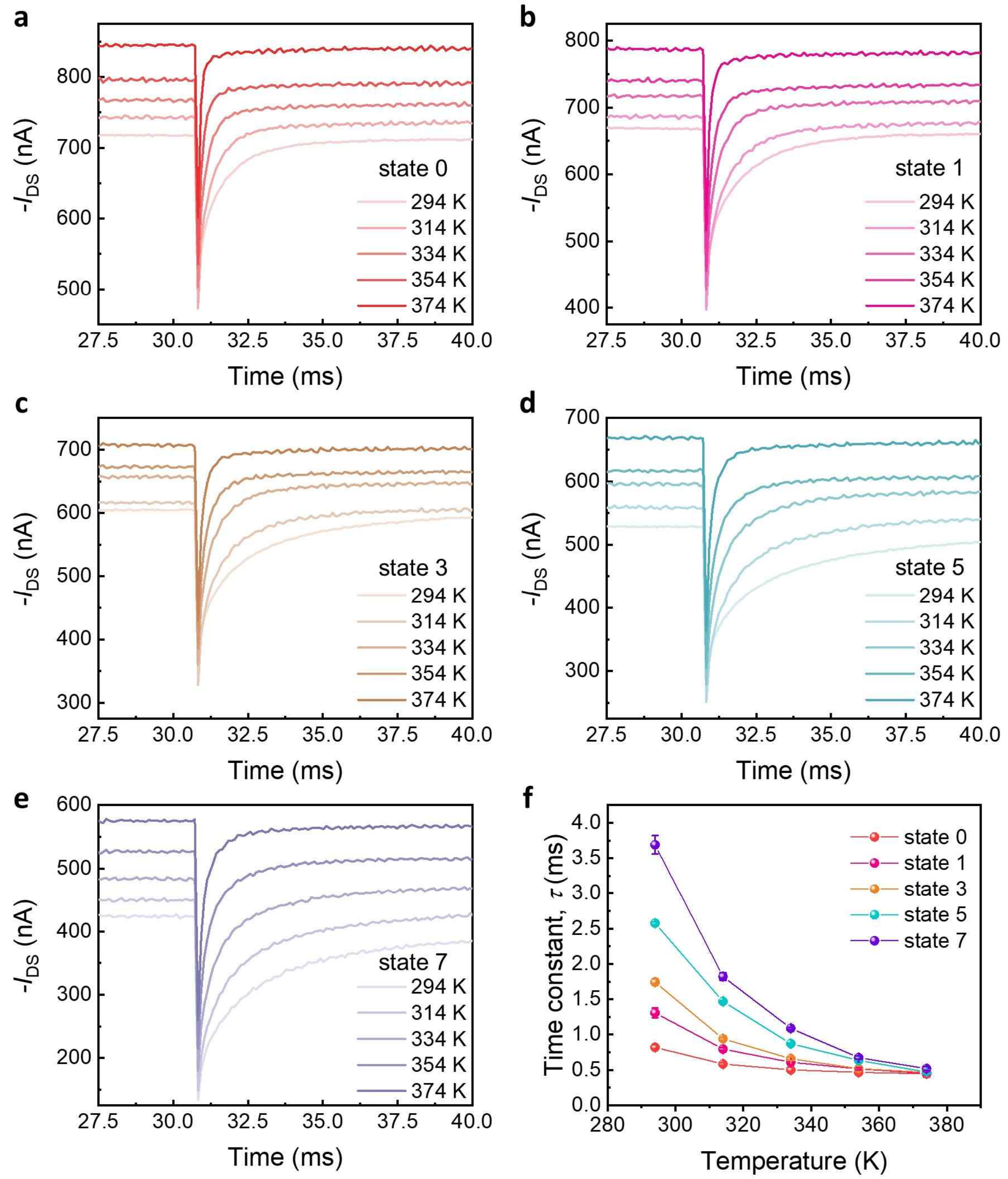

Supplementary Figure 24. Temperature-dependent current responses to a single gate pulse. Current responses to single gate pulse (5 V, 150 ns) with various temperatures from CTL-programmed to **a**, state 0 **b**, state 1 **c**, state 3 **d**, state 5 **e**, state 7 with -2.5 V drain bias. **f**, Calculated time constants at various temperatures. The data were achieved 5 times for each temperature condition and are presented as mean values with error bars indicating standard deviation.

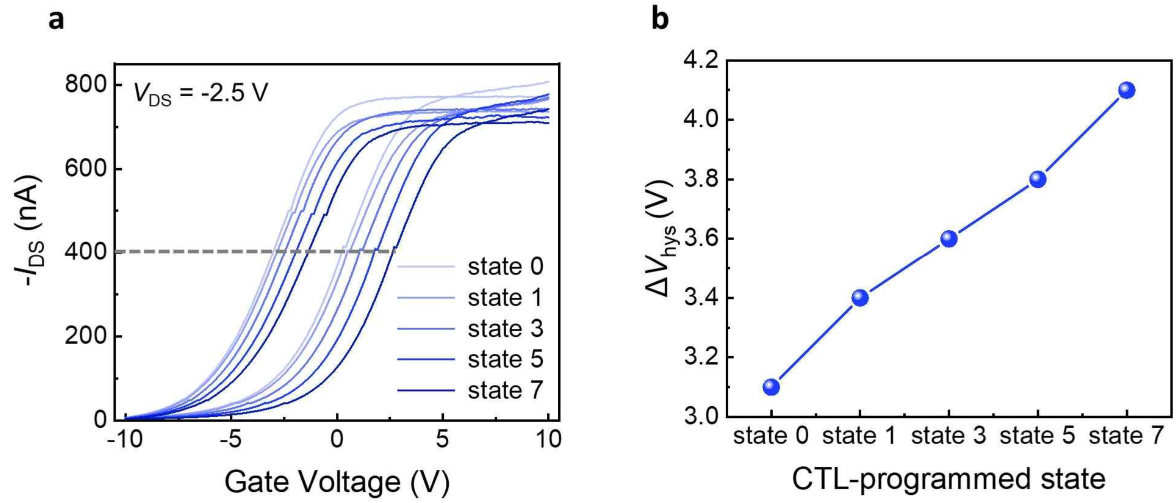

Supplementary Figure 25. Transfer characteristic curves of PDMs with different CTL-programmed states. a, Transfer curves of PDMs with different CTL-programmed states. **b**, Estimated hysteresis voltage window (ΔV_{hys}) for PDMs. The ΔV_{hys} is defined as the difference in the gate voltage at $-I_{DS}$= 400 nA[5].

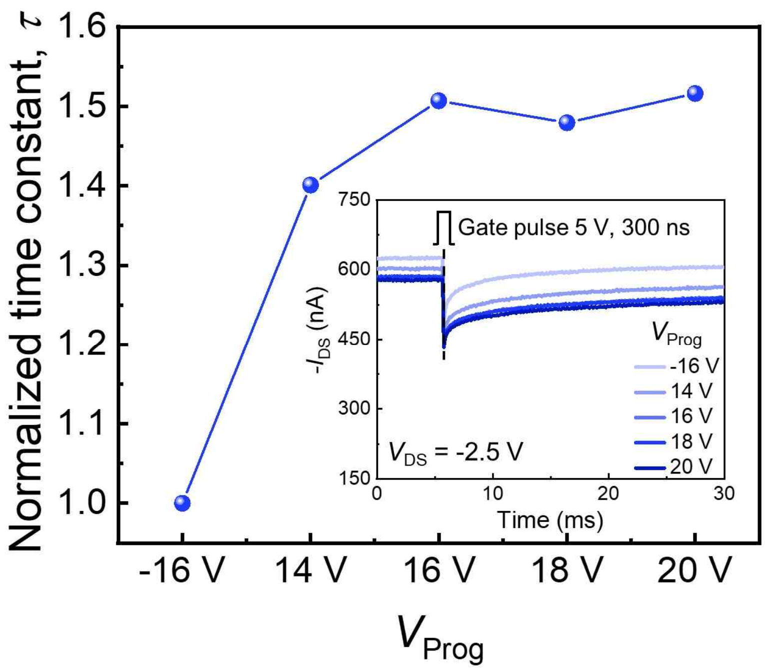

Supplementary Figure 26. Control experiment of a dynamic memtransistor without HfO_2 trapping layer. Change of time constants with varied V_{Prog} pulse (width: 1ms). The inset shows the dynamic current responses to a single gate pulse (5 V, 300 ns) of the control memtransistor. The control memtransistor exhibits transient behavior for a nanosecond-scale gate pulse; however, the tunability of temporal dynamic properties is degraded due to the absence of a trapping layer for multiple states. The drain current transient responses were measured with V_{DS} = −2.5 V (source grounded; sampling interval: 100 μs).

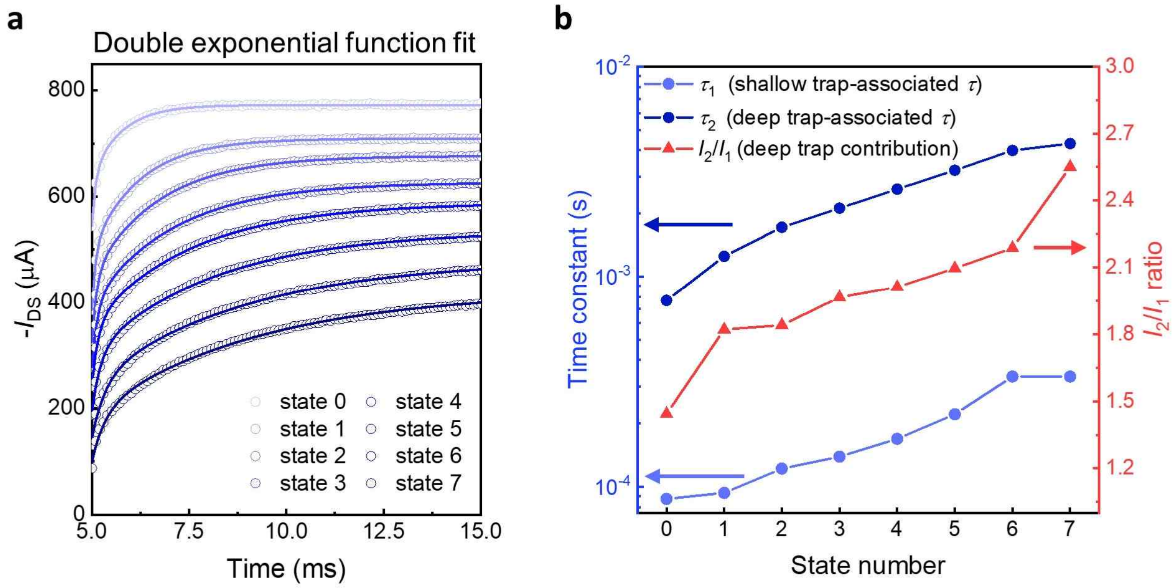

Supplementary Figure 27. Double exponential fitting analysis of single pulse relaxation dynamics across CTL-programmed states. a, Transient drain-current responses of the PDM after a single gate pulse for CTL-programmed states 0–7, fitted using a double-exponential function. The measured relaxation responses were fitted using $I(\mathrm{t})=I_1\exp(-t/\tau_1)+I_2\exp(-t/\tau_2)+I_0$, where τ_1 and τ_2 represent the shorter and longer relaxation time constants, respectively, and I_1 and I_2 are their corresponding coefficients. Open symbols denote experimentally measured drain current, and solid lines denote the corresponding double exponential fit. **b**, Extracted τ_1, τ_2, and I_2/I_1 as a function of CTL-programmed state. The ratio I_2/I_1 quantifies the relative weight of the deep trap component compared with the shallow trap component. With increasing CTL-programmed state, both τ_1 and τ_2 increase, and I_2/I_1 also rises, indicating that deep trap-mediated relaxation becomes increasingly pronounced at higher programmed states. The double exponential fitting shows consistently high quality (average R^2>0.99 across CTL states). These results support a multi-component (shallow/deep trap) nature of the relaxation dynamics, while the single exponential model used in the main text provides an effective time constant for consistent comparison of programmed temporal dynamics across CTL states.

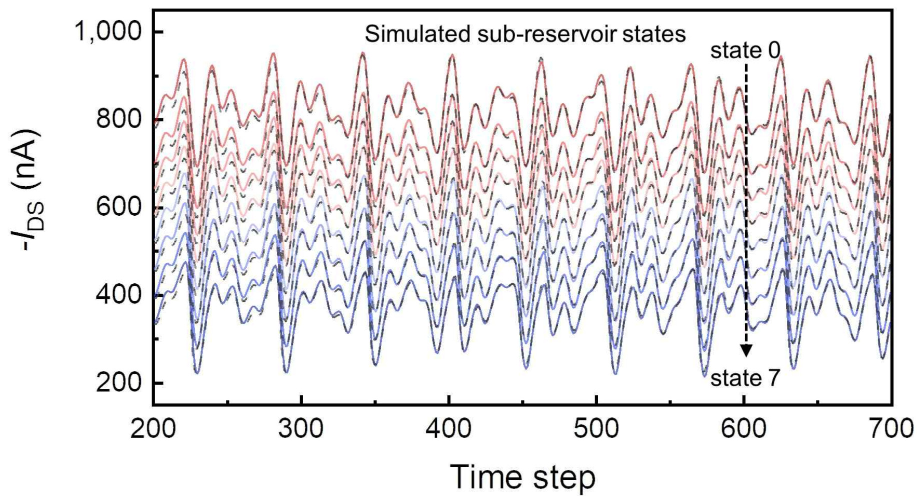

Supplementary Figure 28. Comparison between experimentally measured reservoir states and simulated reservoir states for the MSO task. The physical reservoir states (grey lines) are simulated and plotted based on measured values. Detailed explanations are provided in Supplementary Note 2.

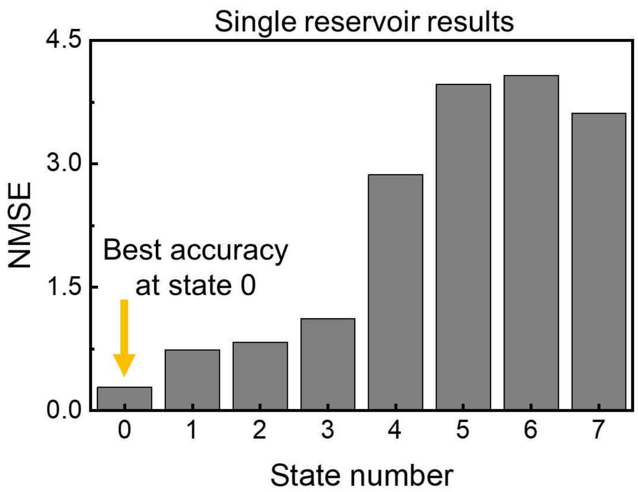

Supplementary Figure 29. State-dependent MSO prediction performance of a single reservoir. NMSE values obtained from the MSO prediction task using a single reservoir configuration, where each CTL programmed state from state 0 to state 7 was used individually. State 0 is the erased state closest to the pristine/as fabricated condition, representing the unmodulated baseline device state before intentional temporal dynamics programming. For fair comparison, the MSO time step length was set to 400 μs by considering the relaxation time constant of state 0, placing the input interval within the effective temporal response window of this baseline single reservoir. Under this condition, state 0 shows the lowest NMSE among the single state reservoir cases, providing the reason for its use as the single reservoir baseline in the comparison with the wide reservoir.

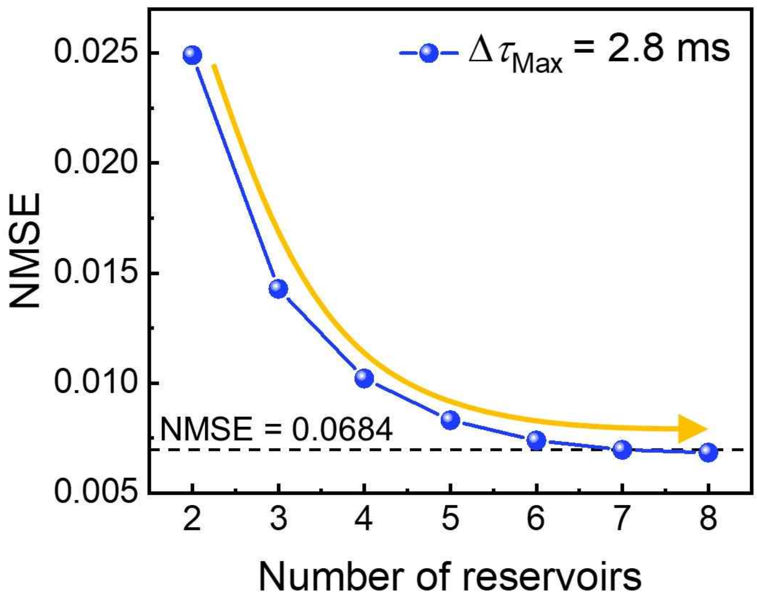

Supplementary Figure 30. Dependence of MSO prediction NMSE on the number of reservoirs. NMSE as a function of the number of reservoirs for a fixed $\Delta\tau_{\mathrm{Max}}$ of 2.8 ms. The results show that increasing the number of reservoirs improves the prediction accuracy, while the performance gain becomes marginal near 8 sub-reservoirs, indicating that the 8-reservoir configuration is already in a near-saturated regime.

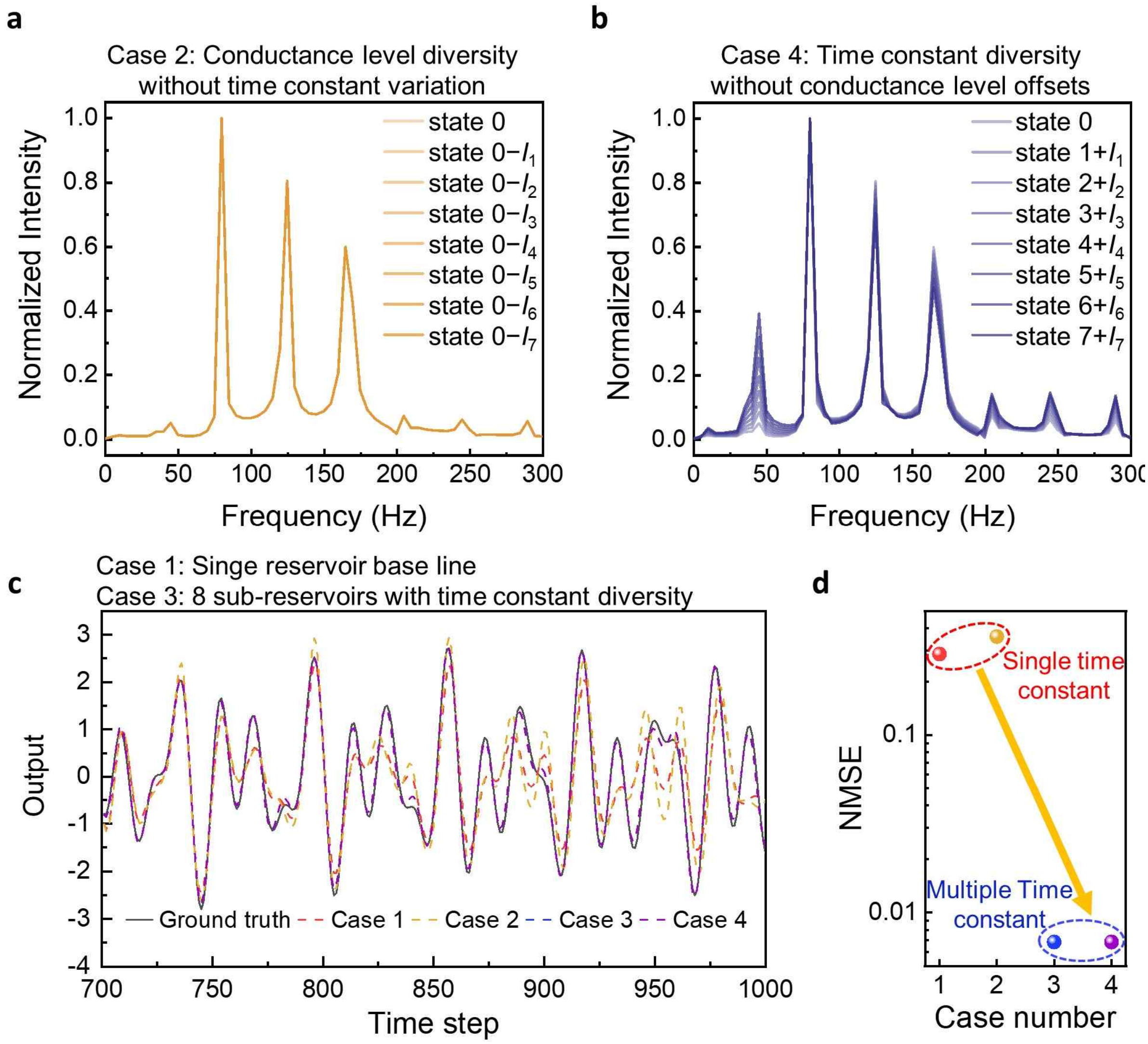

Supplementary Figure 31. Control analysis separating conductance-level offsets from temporal dynamics diversity in the wide reservoir performance improvement. a, Frequency-domain outputs for Case 2, constructed from a single state 0 response with added current offsets (I_1 : 0.09 μA, I_2 : 0.147 μA, I_3 : 0.206 μA, I_4 : 0.266 μA, I_5 : 0.331 μA, I_6 : 0.393 μA, I_7 : 0.452 μA) to mimic conductance-level diversity without τ diversity. **b**, Frequency-domain outputs for Case 4, obtained from the 8 sub-reservoir outputs after offset correction to match the average current level of state 0, thereby suppressing conductance-level offsets while preserving programmed τ diversity. **c**, Representative autonomous prediction outputs for Cases 1–4 compared with the ground truth. (Cases 1 and 3 correspond to the results of the single reservoir and the 8 sub-reservoirs presented in Fig. 4, respectively.) **d**, NMSE comparison for Cases 1–4, showing that conductance-level manipulation alone does not reproduce the performance gain, whereas performance is maintained when τ diversity is preserved.

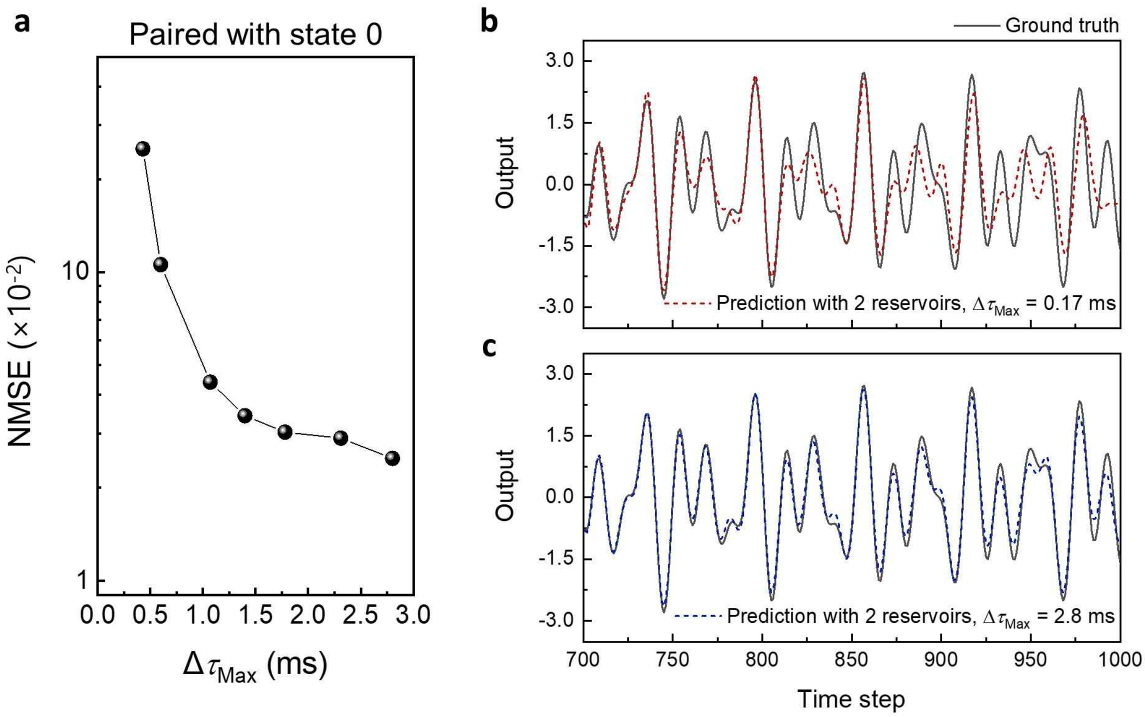

Supplementary Figure 32. Autonomous prediction for the MSO task with 2 sub-reservoirs. **a**, NMSE trend plot with 2 reservoirs paired with CTL erased state (state 0). Prediction results with 2 sub-reservoirs, including state 0 and **b**, state 1 or **c**, state 7. The prediction accuracy improves as the time constant difference between sub-reservoirs increases[6].

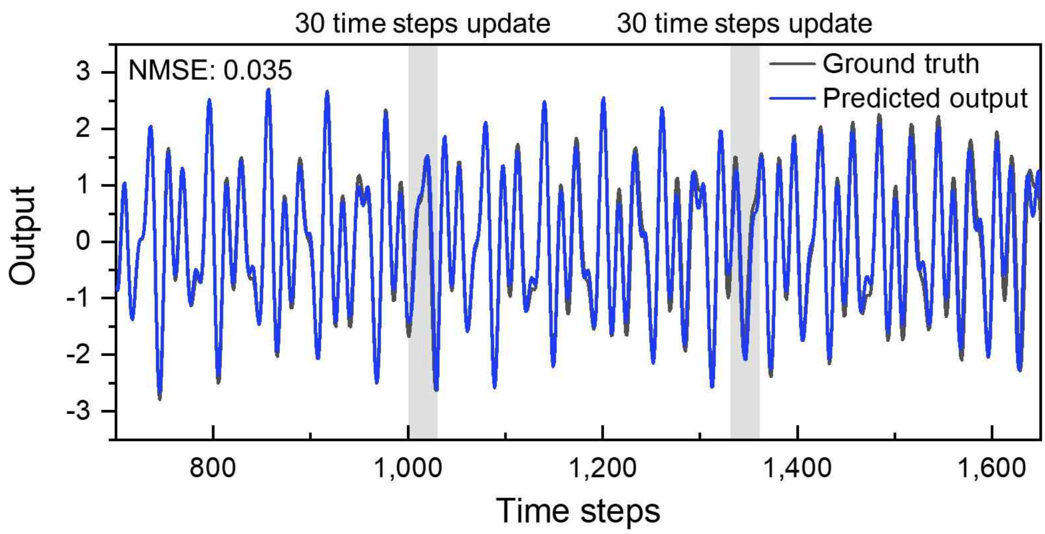

Supplementary Figure 33. Long-term forecasting of the MSO task with periodic updates. The update stage (shaded region, 30 time steps each) is applied after a period of 300 time steps of autonomous prediction and is applied to the true input instead of the predicted value to the reservoir layer.

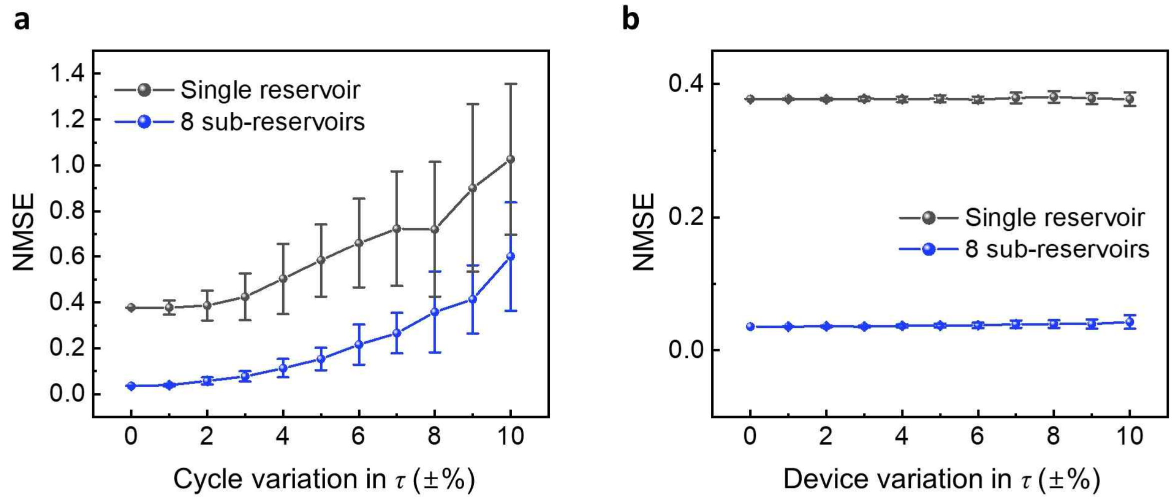

Supplementary Figure 34. NMSE sensitivity analysis of long-term autonomous prediction to variations in the relaxation time constant. a, NMSE as a function of cycle variation in τ for single reservoir and 8 sub-reservoir configurations. **b**, NMSE as a function of device variation in τ for single reservoir and 8 sub-reservoir configurations. Cycle variation causes a more severe accuracy degradation than device variation, while the 8 sub-reservoir configuration maintains a performance advantage over the single reservoir configuration across the examined variation range.

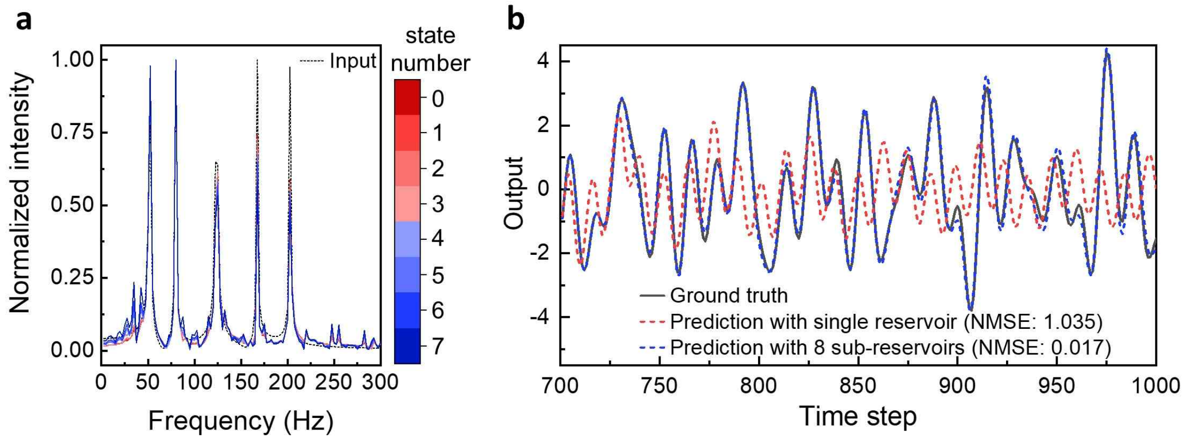

Supplementary Figure 35. Additional MSO prediction task using an input composed of five sinusoidal frequency components. a, FFT spectra of the simulated reservoir outputs for different CTL-programmed states, showing state-dependent spectral emphasis: state 0 exhibits relatively stronger peaks associated with higher-frequency components, whereas higher CTL-programmed states exhibit relatively stronger peaks at lower-frequency components and additional harmonic/intermodulation peaks arising from nonlinear temporal integration. **b**, Representative autonomous prediction trajectories for the MSO input with five frequency components, comparing the single reservoir baseline (state 0 only, NMSE: 1.035) and the wide reservoir configuration using all 8 CTL-programmed states (NMSE: 0.017).

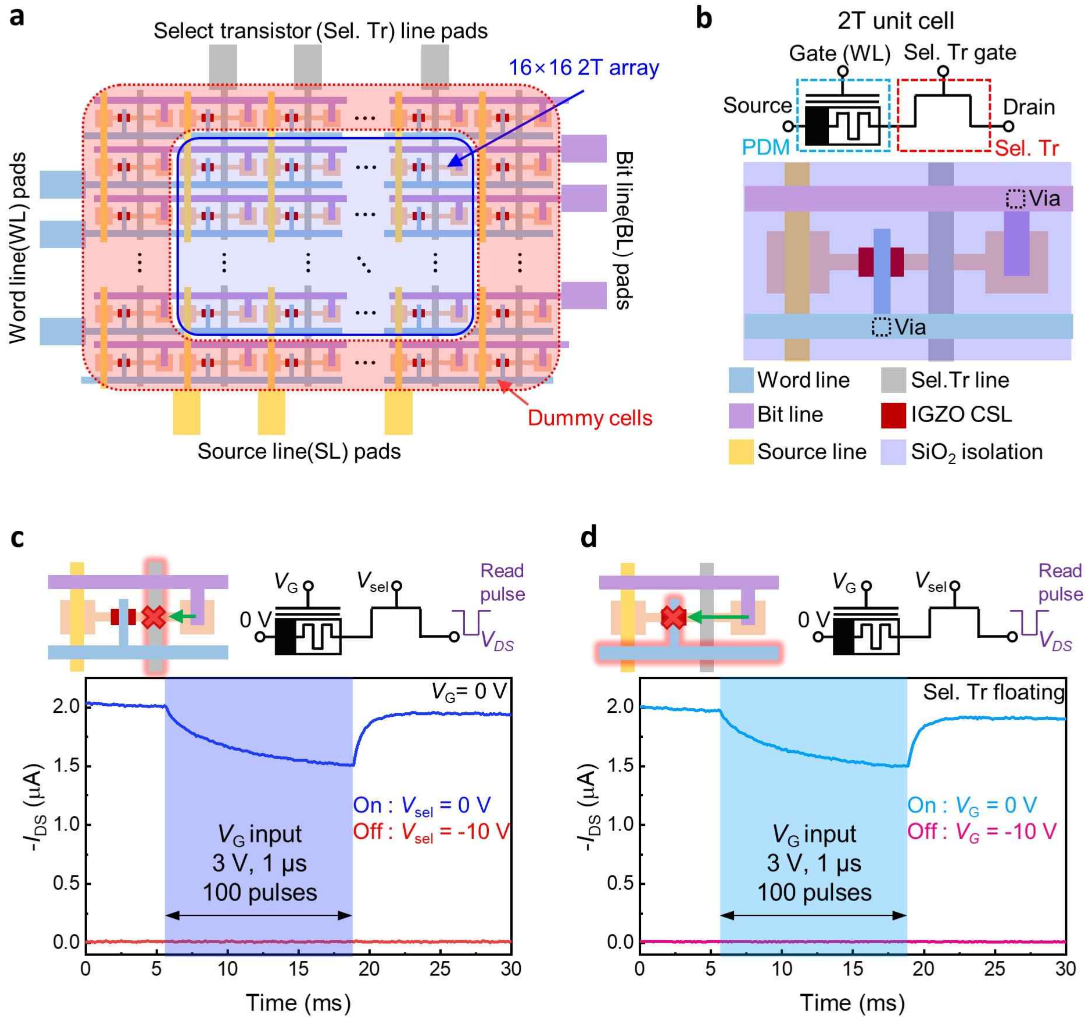

Supplementary Figure 36. Layout and sneak-path suppression scheme of the 16×16 2T PDM array. a, Top-view layout of the 16×16 2T array, showing the active array region and dummy cells. The dummy cells are placed around the active array to mitigate edge-related non-uniformity and are electrically isolated from the active array (no via connections). **b**, Unit-cell layout structure of the 2T cell (1 PDM + 1 select transistor). **c**, Schematic and measured response illustrating column-direction unwanted path suppression by the select transistor under the read operation (with the PDM gate held at V_G=0 V). **d**, Schematic and measured response illustrating row-direction unwanted-path suppression by the PDM transistor operation under the read condition (with the Sel. Tr left floating). In **c** and **d**, the negative bias (V_{sel} = −10 V in **c**; V_G = −10 V in **d**) is applied only during the read operation. The drain current transient responses were measured with V_{DS} = −1 V (source grounded; sampling interval: 120 μs).

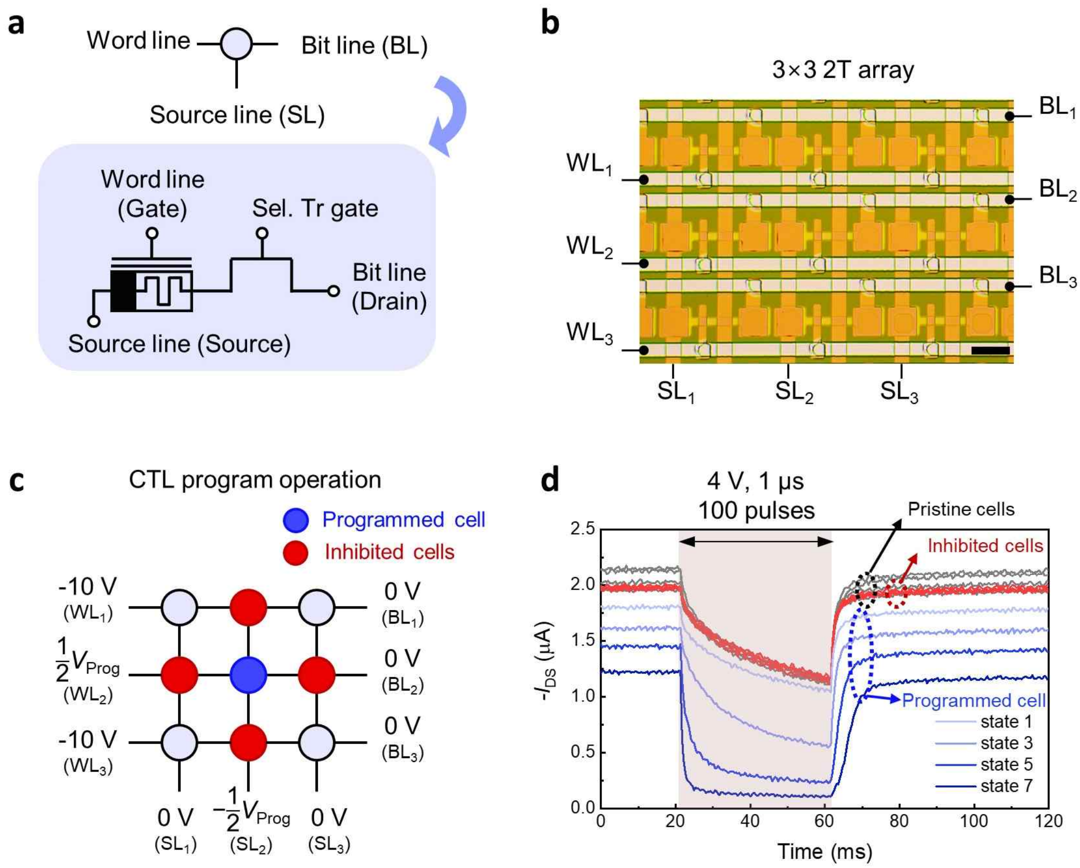

Supplementary Figure 37. The CTL programming operation scheme in the 2T array. a, Simplified unit cell structure. **b**, Optical image of 3×3 2T array. Scales bar, 25 μm. **c**, CTL programming operation biasing scheme. **d**, Dynamic current responses of PDMs in the array after CTL programming operation[7]. To visualize the differences among the CTL-programmed states, 100 gate pulses (4 V, 1 μs) were applied, and the transient drain current responses were measured at $V_{DS} = -1$ V with the source grounded (sampling interval: 400 μs).

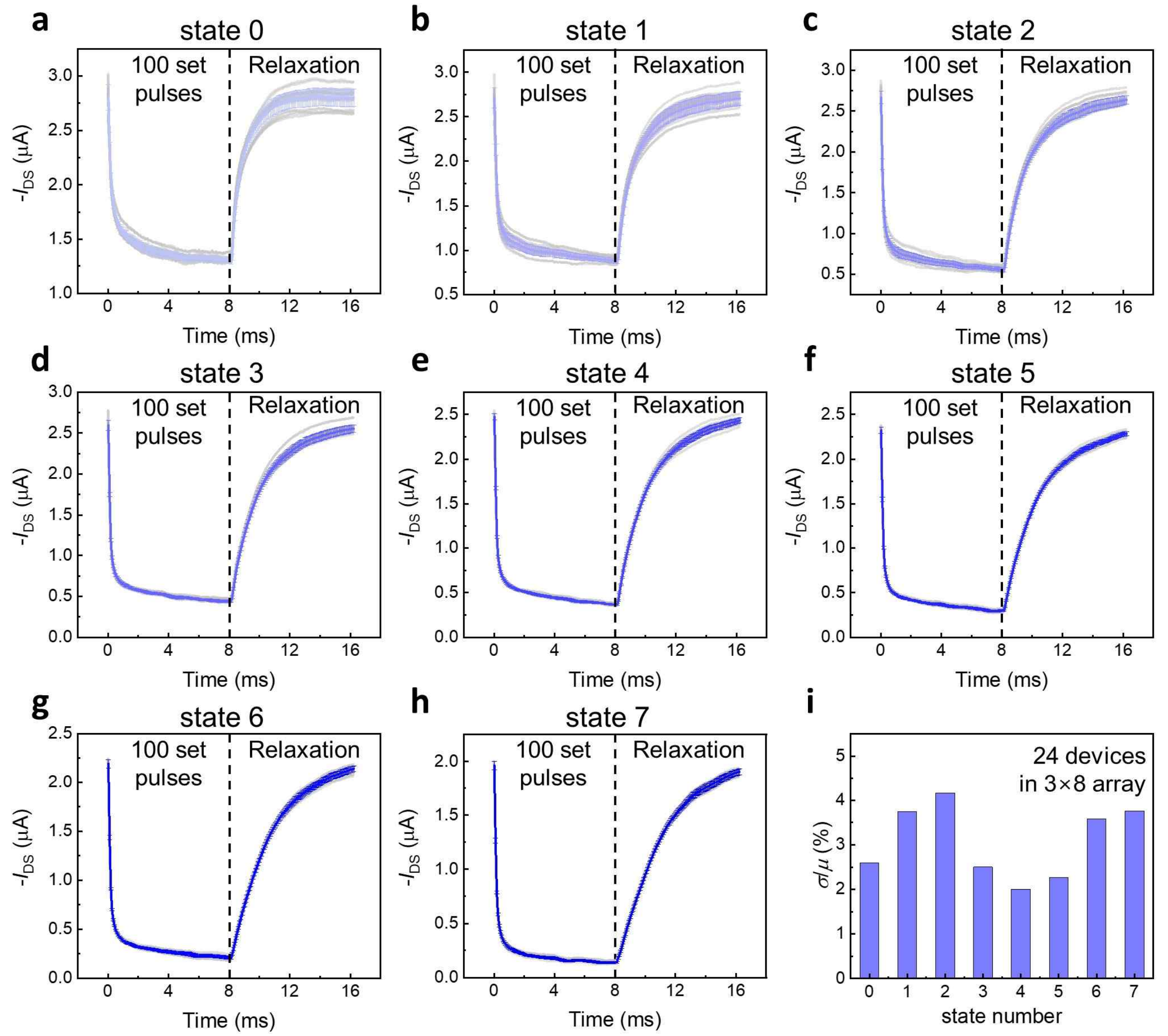

Supplementary Figure 38. Transient current characterization of the 3×8 PDM array. a–h, State resolved current transients measured from the 24 devices (3×8 array) under identical timing definitions, for CTL-programmed states 0–7. A gate pulse train consisting of 100 set pulses (3 V, 1 μs, interval 81 μs) was applied, followed by a relaxation window with the gate held at 0 V. Drain read pulses (−1 V, 50 μs) were applied with a fixed delay of 15 μs after each gate segment to monitor the current response during both the set pulse and relaxation periods. The measured transients show consistent state-dependent summation and recovery behavior across devices, with slower recovery in the relaxation segment as the programmed state increases. In each panel, the gray traces represent the individual device measurements, while the colored trace indicates the average response across devices and the error bars indicate the standard deviation across devices. **i**, The corresponding device variation of the current dynamic. The device variation of the full transient response remains within <5% across the 24 devices under this protocol.

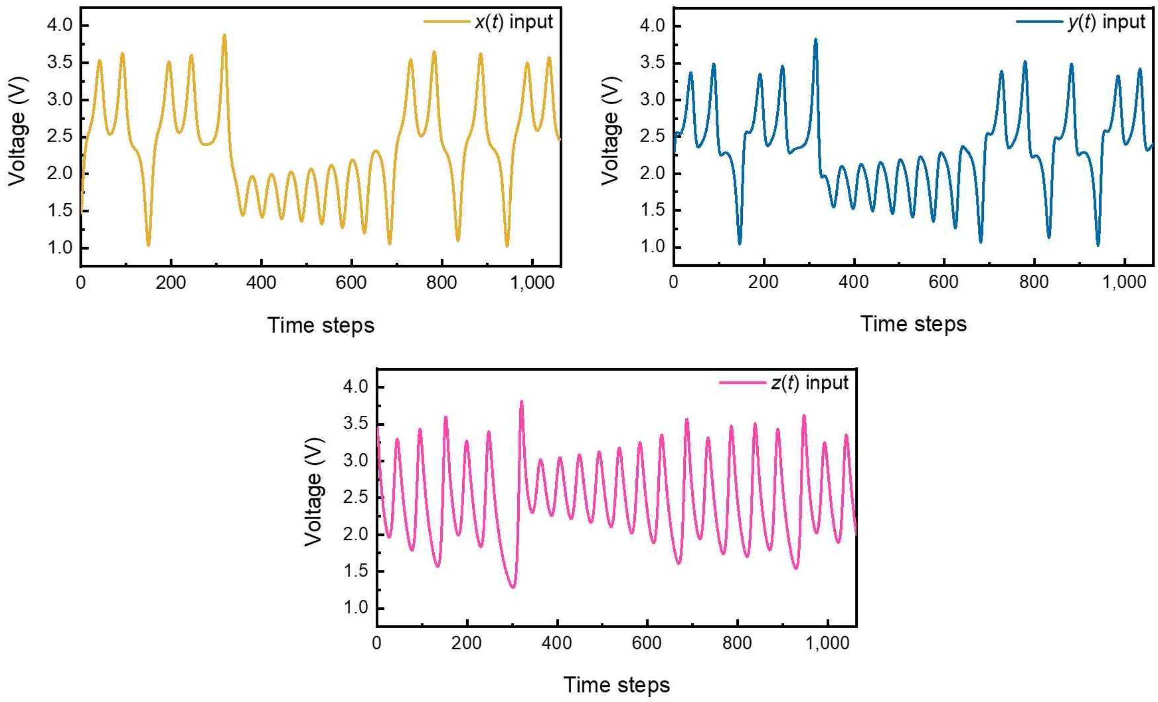

Supplementary Figure 39. One-dimensional time-dependent Lorenz attractor over time deconvoluted from the 3D Lorenz attractor. $x(t)$, $y(t)$, and $z(t)$ input signals were linearly mapped within the range of 1 to 4 V. Each voltage input $x(t)$, $y(t)$, and $z(t)$ was applied to the 1×8 2T arrays, respectively.

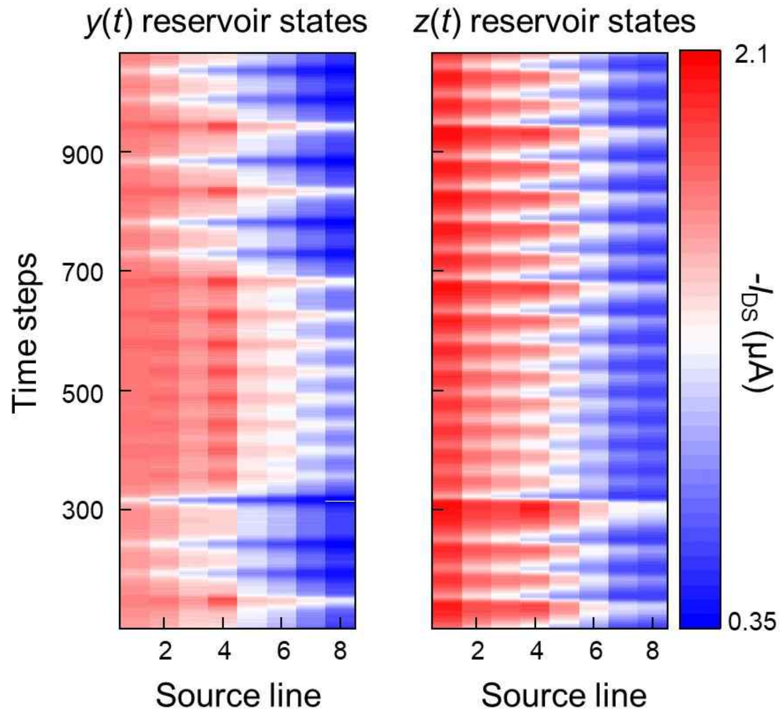

Supplementary Figure 40. Output reservoir states from the 2×8 array functioning as wide reservoirs, for *y*(t) and *z*(t) input pulse streams derived from the Lorenz attractor. Given the respective *y*(t) and *z*(t) inputs, the two PDM 1×8 arrays can produce enriched reservoir states due to their distinct CTL-programmed states.

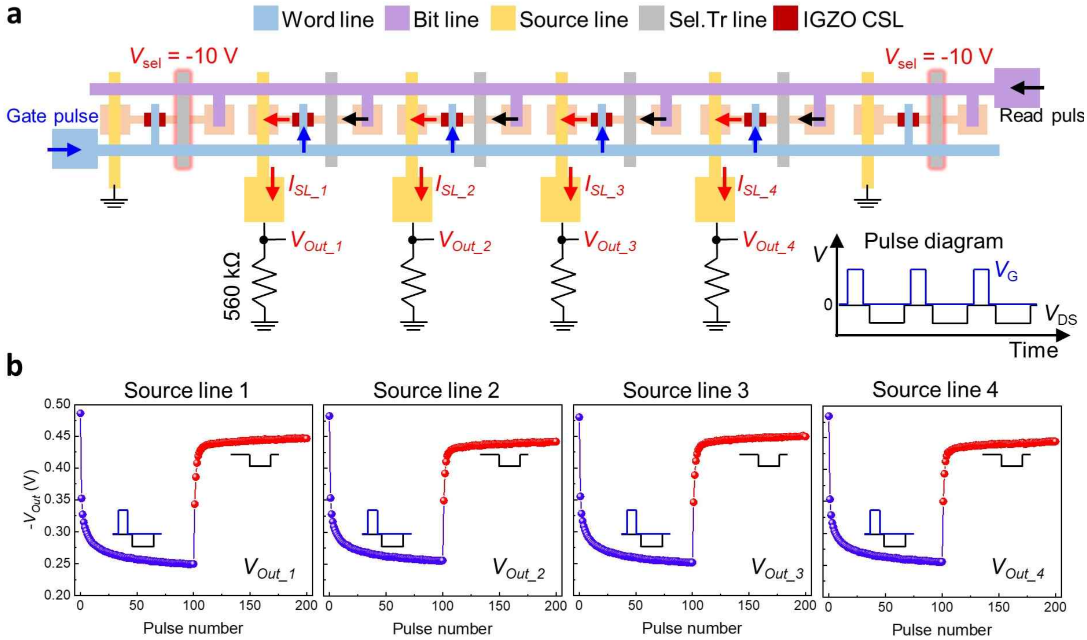

Supplementary Figure 41. Supporting demonstration of row-wise parallel feature extraction in a 1×16 structure. a, Simplified schematic of the row-wise parallel-readout test configuration. 4 cells in a 1×16 row were selected for readout, while adjacent cells on both sides were turned off by the select transistors. A common word line input was applied to the selected row, and output voltages were monitored from the 4 selected source line channels. **b**, Temporal response signals measured from the 4 selected cells (state 0) in the 1×16 row structure under a common word line input. A gate pulse train consisting of 100 repeated gate pulses (3.5 V, 20 μs, interval 1.24 ms) was applied, and the cell responses were monitored using drain read pulses (−1 V, 200 μs) applied with a fixed delay of 20 μs after each gate segment. After the 100 gate pulses, the subsequent spontaneous relaxation was monitored while the gate was held at 0 V. Owing to the measurement-system constraint of this test setup (a single ADC channel in the DAQ), the responses were acquired in the voltage domain rather than by simultaneous multi-channel current readout. The measured signals show parallel temporal outputs from the selected cells under the common word-line input, supporting the feasibility of row-wise parallel feature extraction. The same row-wise routing and selection scheme can be extended to the 8 sub-reservoirs operation used in the wide RC architecture.

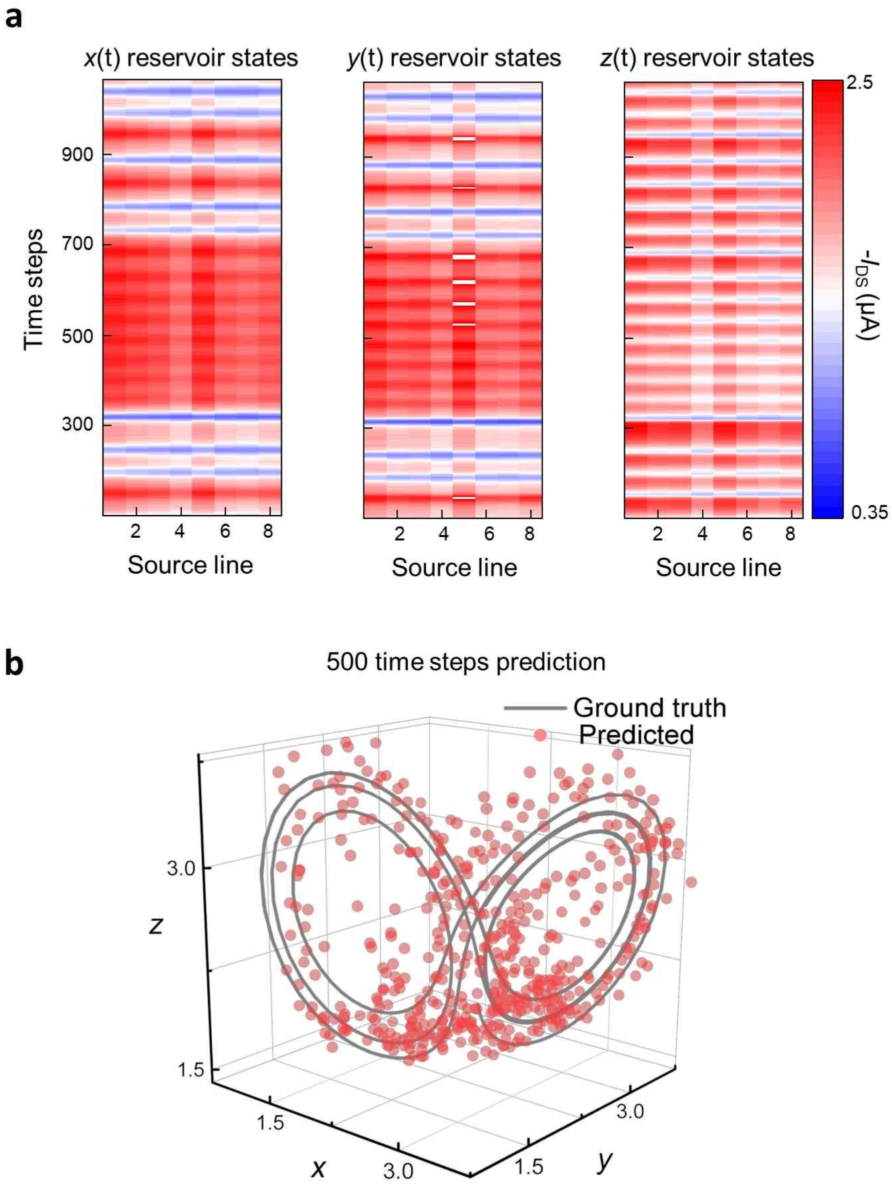

Supplementary Figure 42. Lorenz attractor prediction with a single CTL state. a, Output reservoir states from the 3×8 array for $x(t)$, $y(t)$ and $z(t)$ input pulse streams derived from the Lorenz attractor. The collected reservoir states are qualitatively similar, but quantitatively different due to device variations. **b**, 3D Lorenz attractor prediction results with single CTL state (state 0).

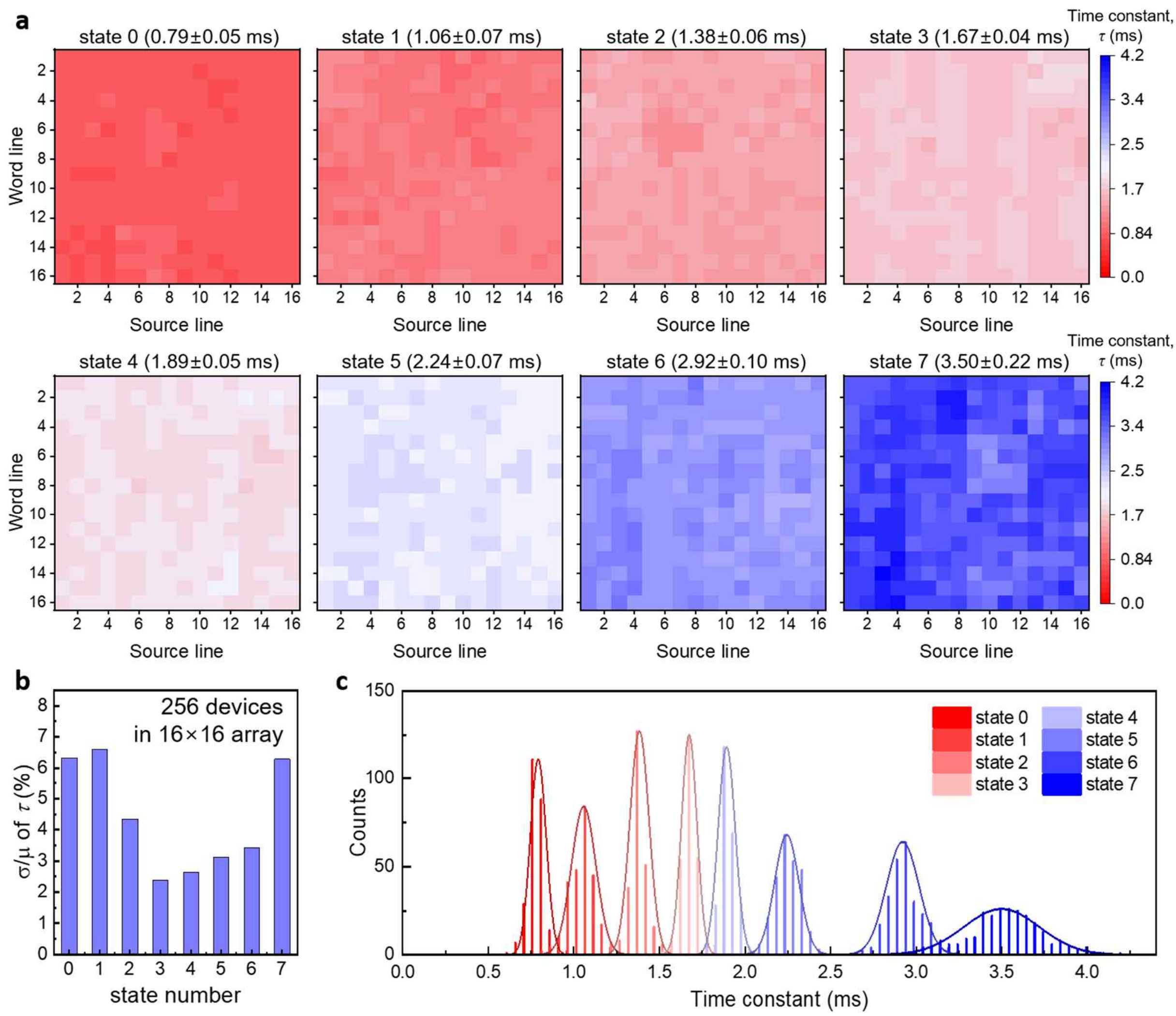

Supplementary Figure 43. Time constant statistics of the 16×16 PDM array. a, State-wise τ maps over the full 16×16 array (256 devices), where each pixel corresponds to a physical device location; τ was extracted using the same pulse/measurement protocol and timing definition as in Supplementary Figure 38. **b**, Device variation of τ across all 256 devices for each CTL-programmed state, showing <7% (σ/μ) within each state. **c**, Probability distributions of τ for states 0–7, showing limited overlap between adjacent states while preserving overall state ordering across the array.

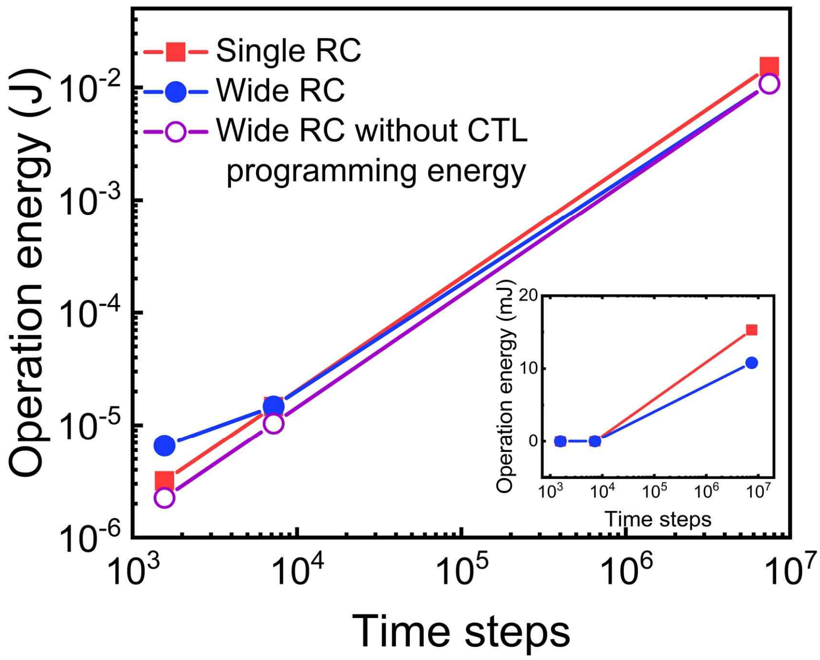

Supplementary Figure 44. Comparison of accumulated operation energy between single RC and wide RC as a function of time steps. Total operation energy of the single RC and wide RC configurations as a function of the number of time steps for the Lorenz attractor prediction task. The accumulated energy includes the array read energy during operation and the one-time CTL programming energy for the wide RC configuration. At short operation lengths, the wide RC shows a higher total energy due to the additional CTL programming overhead. However, because the per-step operation energy of the wide RC is lower, the total energy approaches that of the single RC as the operation length increases. The magenta curve represents the wide RC excluding the one-time CTL programming energy, illustrating the contribution of the programming overhead. The inset highlights the long-operation regime, where the total energy of the wide RC becomes lower than that of the single RC.

Scheme	Single RC (state 0 only)	Wide RC (states 0–7)
Number of devices	24	24 (states 0–7)×3
NMSE	1.2×10^{-2}	2.8×10^{-3} (4-fold improvement)
1 device read energy / time step	8.5×10^{-11} J	6.0×10^{-11} J (average value across 8 CTL-programmed states)
CTL programming energy (as pre-processing)	No energy consumption	4.33×10^{-6} J (total for 24 device configuration)
Total energy for 1,564 steps (0.627 s)	3.19×10^{-6} J	6.58×10^{-6} J
Total energy for 7,221 steps (2.90 s)	1.47×10^{-5} J	1.47×10^{-5} J
Total energy for 7.48×10^{6} steps (3,000 s)	1.53×10^{-2} J	1.08×10^{-2} J

Supplementary Table 1. Comparison of PDM array operation energy and prediction accuracy for single RC and wide RC schemes in multivariate Lorenz attractor prediction. Energy values were estimated for the Lorenz prediction task under identical single RC and wide RC conditions. One-time step corresponds to 401 μs, so 1,564 steps correspond to 0.627 s. Because the gate current is negligibly small, the write operation energy and the gate-side CTL-programming energy were neglected. Therefore, the comparison includes only the cumulative read energy and the channel-side CTL-programming energy of the selected cell under the array-level half-bias scheme. For the read energy calculation, the average measured drain current was used across all 24 devices. For a short operation length of 1,564 time steps, the wide RC scheme consumes more total array operation energy than the single RC scheme. As the operation length increases, however, the energy difference between the two schemes gradually decreases, and the total energy consumption becomes comparable at 7,221 steps (2.90 s) because the wide RC scheme exhibits lower read energy per time step. Over the experimentally demonstrated retention window (3,000 s; 7.48×10^{6} steps), the wide RC scheme is expected to consume less total array operation energy than the single RC scheme. This trend reflects the non-volatile nature of the CTL-programming strategy, which allows the modulated temporal dynamics retained without additional programming energy during repeated reservoir operation.

	Devices (Structure)	Realization of multiple temporal dynamics				Program pulse width [μs]	Total power consumption per input [μW]	Write energy per input [nJ]	Read energy per input [nJ]	CMOS compatibility	Computation Task
		Method	Pre-process	Modulation range	Non-volatile tunability						
Moon *et al.* [1]	1R ($Pd/WO_x/W$)	Device variations	No	N/A	No	300	50	3	0.48	No	Spoken digit recognition, Mackey-Glass prediction
Choi *et al.* [2]	3D-stacked 1R ($Pt/WO_x/W$)	Device variations & 3D structure	No	N/A	No	0.2	18	3×10^{-3}	6×10^{-3}	No	Cell position classification, Lorenz attractor prediction
Zhong *et al.* [11]	1R ($Ti/TiO_x/TaO_y/Pt$)	Mask layer	Yes	N/A	No	120	50	6	N/A	No	Spoken digit recognition, Waveform classification, Hénon map predication
Liu *et al.* [17]	1T FeFET	Mask layer	Yes	N/A	No	6×10^{6}	0.02	0.6	120	Yes	Handwritten digit classification, Voice recognition, Waveform classification, Hénon map predication
Kim *et al.* [18]	1T FeFET	Mask layer	Yes	N/A	No	100	0.2	N/A	0.0225	Yes	COVID-19 cases prediction, Waveform classification, Hénon map predication
Yoo *et al.* [12]	1R (Entropy-stabilized oxide)	Oxide layer composition control	No	~1.75	No	1×10^{3}	0.2	3.4×10^{-3} (Write+Read)		No	Spoken digit recognition
Liu *et al.* [3]	1R (α-In_2Se_3)	Back gate voltage	No	~10	No	5×10^{4}	1.2	N/A	0.1	No	Image classification, Multiple superimposed oscillator prediction
Mun *et al.* [6]	1T (SnO TFT)	Gate voltage & Drain voltage	No	~2.3	No	100	0.02	1×10^{-5}	0.02	Yes	Image classification, Mackey-Glass prediction
Chen *et al.* [13]	1T (IGZO TFT)	Gate voltage	Yes	~100	No	5	0.002	N/A	N/A	Yes	Human activity recognition, Subject trajectory recognition
Lee *et al.* [14]	1T (MoS_2 TFT)	External Gate pulse	No	N/A	No	1×10^{4}	N/A	N/A	N/A	No	Handwritten digit classification
Liu *et al.* [15]	Double gate 1T (ITO TFT)	Second gate voltage	No	~100	No	1×10^{4}	6.5	3×10^{-3}	160	No	Handwritten digit classification, NARMA2 task
Lee *et al.* [19]	1T (MoS_2 TFT)	Gate voltage	No	~8	No	5×10^{3}	0.5	N/A	5	No	Image classification
This work	1T (Silicon channel FET)	Charge trap layer	No	~5	Yes	0.3[a] 1[b] 0.5[c]	1.1[a] 1.2[b] 1.3[c]	7×10^{-12} [a] 3×10^{-11} [b] 2×10^{-11} [c]	0.6[a] 0.06[b] 1.3[c]	Yes	Multiple superimposed[a] oscillator prediction, Lorenz attractor prediction[b], Handwritten digit classification[c]

Supplementary Table 2. Comparison with the various dynamic memristors with tunable temporal characteristics for reservoir computing. Total power and write/read energy are calculated for a single device.

Supplementary Note 1. Details of N-MNIST classification with PDM reservoir

We performed an N-MNIST classification study using experimentally measured PDM current responses to evaluate the applicability of the PDM to a temporally structured classification task. In this analysis, the inter-frame interval was treated as the input temporal scale (Δt), and the primary objective was to examine how programmable PDM temporal dynamics enable multiscale temporal feature extraction across different input temporal scales.

As a basis for feature construction, we first measured PDM current responses to 16 different 4-bit temporal input sequences (codes 0000–1111) across multiple input temporal scales (Δt = 0.5, 1, 2, 3, 4, and 5 ms) and 8 CTL-programmed states (states 0–7) (Supplementary Fig. 19 and 20). The measured response distributions show that the separability among the 16 sequence responses changes systematically with both Δt and CTL-programmed state, indicating that the programmed temporal dynamics influence how temporal input patterns are represented in the final current response.

Using these experimentally measured responses, we then constructed reservoir features for N-MNIST classification (Supplementary Fig. 21a). The N-MNIST event data (34×34 images) (Orchard *et al.*)[20] were converted into a 4-frame representation, binarized with a fixed threshold, and encoded into pixel-wise 4-bit sequences (0000–1111). For a selected Δt and CTL-programmed state, each pixel-wise 4-bit code was mapped to the corresponding experimentally measured PDM current value, thereby generating a 34×34 reservoir-state map for classification[21]. The classification accuracy was evaluated for each Δt/state condition using a separately trained readout, allowing direct comparison of how different programmed PDM states process input data with different temporal scales.

To analyze how temporal information is encoded in the experimentally measured 16-sequence response set, we additionally performed linear regression-based analyses using the coefficient of determination (R^2) as a metric (Supplementary Fig. 21b,c). For each (Δt, CTL-programmed state) condition, a 16-point response vector, $y = [I_0, I_1, ..., I_{15}]$, was constructed from the experimentally measured responses corresponding to the 16 input codes. We then evaluated how strongly this measured response distribution can be explained by simplified descriptors of the 4-bit code using linear regression. For a given response vector, y (16×1), the fitted model is written as $y = X\beta + e$, (X is the explanatory-variable matrix (with intercept), β is the fitted coefficient vector, and e is the residual error term) and the coefficient of determination is calculated as $R^2 = 1 - SSE/SST$, where SSE is the residual sum of squares and SST is the total sum of squares of y.

Two simplified models were used:

1. Last-bit-only model (R^2_lastbit): the explanatory variable contains only the least significant bit (LSB) of each 4-bit code. Because the 4-bit code is derived from a 4-

frame representation, the LSB corresponds to the 4th frame (the most recent temporal segment).

2. Popcount-only model (R^2_popcount): the explanatory variable contains only the popcount (the number of active bits in the 4-bit code), which preserves the total number of active frames/pulses but discards temporal order.

Accordingly, these two R^2 metrics provide complementary information on the dominant sequence separation rule in the experimentally measured responses. A high R^2_lastbit indicates that the measured responses are predominantly determined by the most recent-frame information (last-bit dominance), whereas a high R^2_popcount indicates that the measured responses are predominantly determined by total activity level (popcount dominance) with reduced sensitivity to sequence order.

The heat maps in Supplementary Figure 21b,c show that these tendencies vary systematically with Δt and CTL-programmed state. Specifically, last-bit dominance (high R^2_lastbit) tends to increase at longer Δt and lower CTL-programmed states, while popcount dominance (high R^2_popcount) tends to increase at shorter Δt and higher CTL-programmed states. This behavior is consistent with the Δt-dependent interplay between temporal summation and relaxation under different programmed temporal dynamics: at longer Δt and shorter relaxation time constants (lower states), earlier pulse contributions decay more strongly before readout, making the final response more dependent on the most recent bit; in contrast, at shorter Δt and longer relaxation time constants (higher states), pulse overlap and temporal integration are enhanced, making the final response more dependent on the total number of active inputs.

These results indicate that the experimentally measured 16-sequence responses do not preserve temporal-input information in a single fixed manner. Rather, both the dominant sequence-separation mode and the overall sequence discriminability change with Δt and CTL-programmed state. In this sense, Δt and the programmed PDM temporal dynamics jointly determine the sequence-separation characteristics of the measured response space.

The corresponding N-MNIST classification results are shown in the Supplementary Figure 21d. For each Δt condition, there exists an optimal CTL-programmed state range for classification, and this optimal range shifts with Δt. As Δt increases, the higher accuracy region tends to move toward larger CTL-programmed states, consistent with the need for longer temporal memory (larger τ). This indicates that the classification performance depends on matching the input temporal scale to the programmed PDM temporal dynamics.

Importantly, in this N-MNIST evaluation, each sample was represented with a uniform input temporal scale (Δt) for a given condition. Under this setting, the observed Δt-dependent shift of the optimal CTL-programmed state range indicates that differently programmed PDMs' time constants preferentially extract task-relevant features from different temporal-scale regimes of the input data. In this sense, the present N-MNIST study provides application-level evidence that programmed temporal diversity enables multiscale temporal feature extraction in temporally structured tasks (Supplementary Fig. 21e).

These results support that the programmable temporal dynamics of the PDM provide a practical route to match reservoir responses to the temporal scale of the input signal. More broadly, a reservoir platform composed of PDMs spanning a wide range of programmed time constants can cover diverse temporal scale regimes and thereby enable multiscale temporal feature extraction with robust performance across temporally diverse classification tasks[12,13].

Supplementary Note 2. Device modeling for time-series data prediction.

The conductance of the PDM originates from free electron density in the Si channel[8]. The PDM's volatile resistive switching behaviors are attributed to the electron trapping and de-trapping in the CSL region[9]. The device's characteristics exhibit distinct transient and recovery phases, which can be accurately described using a piecewise function[10]. When positive voltage pulses are applied to the gate, the drain current ($I(t)$) is decreased on a nanosecond scale, which is affected by the past conductance state (Eq. (1)). After the removal of the gate voltage, the drain current spontaneously recovers according to Eq. (2).

$$\Delta I(t) = I(t-1)\alpha[\exp(V-\beta)] \qquad (1)$$

$$I(t) = I(t-1) + \Delta I(t) + \omega[\exp\left(-{}^{t}/_{\tau}\right)] \qquad (2)$$

where V is the gate voltage input, t is the time, and τ is the time constant. For different CTL-programmed states, the τ is used from experimentally measured values, and other hyperparameters (α, β, and ω) are numerically fitted based on experimental data, as shown in Supplementary Figure 28. Based on fitting results, the prediction task of the wide physical RC was performed.

The diversified volatile resistive switching dynamics across different CTL-programmed states enable the formation of varied sub-reservoir nodes within the wide physical reservoir layer. The modulation of temporal dynamics is verified through measurements using gate voltage and identical pulse inputs, as demonstrated in Supplementary Figure 7, which highlights the distinct transient responses under various CTL-programmed states.

Supplementary Note 3. The merit of the PDM array-based RC system.

There have been several strategies to achieve diverse temporal dynamics at the hardware level, thereby expanding reservoir dimensionality and enhancing the performance of RC. For instance, input masking involves multiplying the input signal by a sequence of binary or analog values across subdivided time intervals[11].

However, implementing this technique requires additional peripheral circuitry, such as multiplexers and mask generators at each device node, which increases system complexity and energy consumption and limits scalability in large-scale hardware implementations[16].

Additionally, approaches such as compositional tuning[12] of resistive switching materials and utilizing inherent device variation[1,2] can modulate relaxation time constants and induce diverse short-term memory behaviors, but suffer from limited post-fabrication tunability and high fabrication complexity.

Some previous studies based on three-terminal devices have demonstrated that applying a constant gate bias can accelerate or decelerate transient dynamics by influencing charge trapping/de-trapping or ion migration processes[3,6].

However, this method is only valid while the bias is constantly applied; thus, the modulated state cannot be stored in a non-volatile manner and leads to continuous power consumption. Furthermore, this method lacks scalability, particularly at the array level, where the gate electrode is typically shared across multiple devices.

In contrast, PDM offers the controllable temporal dynamics in a non-volatile manner, which can be modulated by electron density in CTL. PDM exhibits the tunable relaxation time constants with a 5-fold modulation range and can be programmed in 8 reservoir states, enabling the construction of a wide physical reservoir layer without the need for input preprocessing. This capability significantly enhances computational capacity and allows real-time processing. Thanks to the intrinsic tunability of temporal dynamics, PDM devices can be scaled to array-level implementations and process the multi-variable temporal input in parallel. Because the temporal states are configured by non-volatile CTL programming, the added overhead is a one-time pre-configuration step (rather than a per-input operation). Combined with fast operation speed (50 ns), low write operation energy (0.21 aJ per 100 inputs), and CMOS compatibility, our approaches provide a promising RC platform for high-precision and low-latency in edge computing systems.

Supplementary Note 4. Prospective applications of PDM beyond reservoir computing

The present work demonstrates the PDM as a programmable multiscale physical reservoir for RC. More generally, the key functionality of the PDM is non-volatile programmability of temporal dynamics, namely the ability to set distinct relaxation time constants (τ) via CTL charge storage. Because many neuromorphic functions rely on time-domain operations (temporal integration, decay, filtering, and summation), this device-level programmability may be useful in a broader range of time-domain processing modules beyond the specific RC architecture studied here.

1) Near-sensor computing applications

One prospective direction is near-sensor neuromorphic computing. When the output of a sensor is directly applied to the PDM gate as a time-varying input signal, the programmed τ of PDM can modulate the temporal summation and filtering of the sensor-derived signal according to its temporal frequency content[23,24]. In this way, PDM can operate as a programmable temporal front-end element that performs hardware-level temporal encoding before higher-level processing. For example, by tuning the temporal integration window to the characteristic timescale of the input signal, the system may support motion/path extraction that is less sensitive to variations in object speed.

2) Artificial dendritic or neuronal processing blocks

In neuromorphic circuits, dendritic/neuron-like response characteristics are often determined by circuit parameters that define integration and decay dynamics[25,26]. Incorporating a device element with programmable τ provides an additional degree of freedom to modulate temporal integration, decay, and response shape, even under the same external circuit configuration. Therefore, PDM can be used as a configurable temporal integration unit in dendrite-inspired or neuron-like computing blocks, where distinct programmed τ states yield different temporal response characteristics without changing external passive components.

These applications are beyond the scope of the present study and would require architecture-specific circuit co-design and experimental validation. Nevertheless, the non-volatile programmability of temporal dynamics in PDM suggests broad potential for time-domain neuromorphic hardware beyond RC.

Supplementary References

1 Moon, J. *et al.* Temporal data classification and forecasting using a memristor-based reservoir computing system. *Nat. Electron.* **2**, 480-487 (2019).

2 Choi, S. *et al.* 3D-integrated multilayered physical reservoir array for learning and forecasting time-series information. *Nat. Commun.* **15**, 2044 (2024).

3 Liu, K. *et al.* An optoelectronic synapse based on α-In2Se3 with controllable temporal dynamics for multimode and multiscale reservoir computing. *Nat. Electron.* **5**, 761-773 (2022).

4 Mativenga, M., Haque, F., Billah, M. M. & Um, J. G. Origin of light instability in amorphous IGZO thin-film transistors and its suppression. *Sci. Rep.* **11**, 14618 (2021).

5 Liao, F. *et al.* Bioinspired in-sensor visual adaptation for accurate perception. *Nat. Electron.* **5**, 84-91 (2022).

6 Mun, S. A. *et al.* High-dimensional physical reservoir with Back-end-of-line-compatible tin monoxide thin-film transistor. *ACS Appl. Mater. Interfaces* **16**, 42884-42893 (2024).

7 Schranghaer, T. F. *et al.* Large-scale crossbar arrays based on three-terminal MoS_2 memtransistors. *Nat. Commun.* **16**, 9518 (2025).

8 Duarte, J. P., Choi, S.-J., Moon, D.-I. & Choi, Y.-K. Simple analytical bulk current model for long-channel double-gate junctionless transistors. *IEEE Electron Device Lett.* **32**, 704-706 (2011).

9 Park, T. *et al.* Ultra-low power and reliable dynamic memtransistor based on charge storage junction FET with step-wise potential barrier for energy-efficient edge computing framework. *Adv. Electron. Mater.* **10**, 2300904 (2024).

10 Liu, Z. *et al.* Interface-type tunable oxygen ion dynamics for physical reservoir computing. *Nat. Commun.* **14**, 7176 (2023).

11 Zhong, Y. *et al.* Dynamic memristor-based reservoir computing for high-efficiency temporal signal processing. *Nat. Commun.* **12**, 408 (2021).

12 Yoo, S. *et al.* Efficient data processing using tunable entropy-stabilized oxide memristors. *Nat. Electron.* **7**, 466-474 (2024).

13 Chen, R. *et al.* Thin-film transistor for temporal self-adaptive reservoir computing with closed-loop architecture. *Sci. Adv.* **10**, eadl1299 (2024).

14 Lee, H. *et al.* Enhancing computing capacity via reconfigurable MoS_2-based artificial synapse with dual feature strategy for wide reservoir computing. *Adv. Funct. Mater.* **35**,

2416811 (2025).

15 Liu, K. et al. A multi-terminal ion-controlled transistor with multifunctionality and wide temporal dynamics for reservoir computing. *Nano Res.* **17**, 4444 (2024).

16 Zhong, Y. *et al.* A memristor-based analogue reservoir computing system for real-time and power-efficient signal processing. *Nat. Electron.* **5**, 672 (2022).

17 Liu, Z. *et al.* Interface-type tunable oxygen ion dynamics for physical reservoir computing *Nat. Commun.* **14**, 7176 (2023).

18 Kim, J. *et al.* Analog reservoir computing via ferroelectric mixed phase boundary transistors. *Nat. Commun.* **15**, 9147 (2024).

19 Lee, K. *et al.* Temporally reconfiguable reservoir computing with flexible electrolyte-gated TFTs for high-performance neuromorphic processing. *Adv. Mater.* **38**, e07979 (2026).

20 Orchard, G., Jayawant, A., Cohen, G. K. & Thakor, N. Converting static image datasets to spiking neuromorphic datasets using saccades. *Front*. *Neurosci*. 9, 437 (2015).

21 Qin, L. *et al*. Molecular crystal memristors. *Nat*. *Nanotechnol*. **20**, 1641–1647 (2025).

22 Lee, K. *et al.* Temporally reconfiguable reservoir computing with flexible electrolyte-gated TFTs for high-performance neuromorphic processing. *Adv. Mater.* **38**, e07979 (2026).

23 Wang, M. *et al*. Tactile near-sensor analogue computing for ultrafast responsive artificial skin. *Adv*. *Mater*. **34**, e2201962 (2022).

24 Chen, Y. *et al*. Capacitive in-sensor tactile computing. *Nat*. *Commun*. **16**, 5691 (2025).

25 Xu, H. *et al*. A low-power vertical dual-gate neurotransistor with short-term memory for high energy-efficient neuromorphic computing. *Nat*. *Commun*. **14**, 6385 (2023).

26 Park, S. O., Jeong, H., Park, J., Bae, J. & Choi, S. Experimental demonstration of highly reliable dynamic memristor for artificial neuron and neuromorphic computing. *Nat*. *Commun*. **13**, 2888 (2022).